

Stability/instability of electrorheological nano pipes used in braking nanosystems by the machine learning method

Sihao Huang, Yuelin Xu & Maoxin Yin

To cite this article: Sihao Huang, Yuelin Xu & Maoxin Yin (20 Jan 2023): Stability/instability of electrorheological nano pipes used in braking nanosystems by the machine learning method, Waves in Random and Complex Media, DOI: [10.1080/17455030.2023.2166687](https://doi.org/10.1080/17455030.2023.2166687)

To link to this article: <https://doi.org/10.1080/17455030.2023.2166687>



Published online: 20 Jan 2023.



Submit your article to this journal [↗](#)



Article views: 76



View related articles [↗](#)



View Crossmark data [↗](#)



Stability/instability of electrorheological nano pipes used in braking nanosystems by the machine learning method

Sihao Huang^{a,#}, Yuelin Xu^{b,#} and Maoxin Yin^a

^aMaterials Science and Engineering, Shenzhen MSU-BIT University, Shenzhen, People's Republic of China;

^bDepartment of Computational Mathematics and Cybernetics, Shenzhen MSU-BIT University, Shenzhen, Guangdong, People's Republic of China

ABSTRACT

Electro-rheological fluids change their viscosity properties due to their application in an electrical field. This property could be acquired and maintained by accurately controlling the external electrical field. Besides brake systems, such electro-rheological (ER) fluids could be utilized in small-scale damping systems. In the present study, for the first time, the effects of using an electrical field in improving the dynamic stability of nanostructure containing ER fluids are presented. In this regard, a cylindrical sandwich structure, with an inner and outer layer composed of two-directional functionally graded (2D-FG) material and ER fluid core, is considered. Employing energy methods and modified power law the equations of motion of the structure are derived. Between FG and ER layers' compatibility conditions are imposed in terms of displacement and strains. Moreover, to bypass computational complications, the inputs and outputs are utilized for training a deep neural network (DNN). In this way, the inputs and outputs are related to each other through the regression method without numerically solving the equations of motion all over again. Finally, the effects of different parameters on the frequency and loss factor characteristics of the current nanostructure will be presented.

ARTICLE HISTORY

Received 13 August 2021

Accepted 27 December 2022

KEYWORDS

ER layer; 2D-FG face sheets; modal loss factor; braking nanosystems; DNN technique

1. Introduction

Applications of nanostructures are growing due to their small dimensions [1,2], low weight, and accuracy in measuring different quantities [3,4]. Composite nanostructures, on the other hand, demonstrated excellent mechanical properties besides other thermal and electrical properties [5–8]. A novel application of such structures is in the small-scale brake systems in which electro-rheological (ER) fluids are used in a cylindrical system. Electro-rheological fluids change their viscosity properties due to their application in an electrical field. This desired property could be acquired and maintained by accurately controlling the external electrical field. Besides brake systems, such electro-rheological fluids could be utilized in small-scale damping systems. The mentioned material can be used in many systems [9–12] and structures [13–16]. Kolekar et al. [17] presented a review article about

CONTACT Yuelin Xu ✉ 1120190060@smbu.edu.cn

[#]Co-first author

the vibration control of flexible structures using the semi-active method associated with smart materials of electrorheological fluids, magnetorheological fluids, and magnetorheological elastomers. They found that both damping and stiffness properties of the sandwich structures could be effectively controlled in several ways: the change of the field intensity, the location of cores zones, the partial and full treatment, and boundary conditions of the structures.

The utilization of electro- and magneto-rheological fluids in the industrial process is widespread from braking systems and suspension devices to health care systems. However, their applications in the nano-/micro-system are new and are continuing to explore [18–23]. Halsay [24] discussed common properties and applications of ER fluids. Hao [25] reviewed articles on the different types and applications of ER. In the review, Hao mentioned the negative ER fluids and predicted great application grounds for these type of fluids. Xu et al. [26] presented an application for ER and magnetorheological fluids in controlling the seismic responses of buildings. They examined the effects of different parameters on the optimal control of vibration in the building during an earthquake. Studying example buildings, they showed that ER dampers were more effective than passive dampers in such buildings. Wei et al. [27] utilized ER fluids in sandwich beams to suppress undesired vibration in rotating beams. The results of the theoretical study demonstrated that the vibration of the beam due to rotation could be effectively reduced. Wei et al. [28] utilized electrical fields to change the ER substrate of beams to control the vibration of the beam. They employed numerical finite element simulations to show the capability of the ER foundation in damping. Moreover, the results of the damping substrate were compared to the core damping in sandwich beams and both ER damping configurations provided similar results. Vishnu Narayana and Ganesan [29] employed ER fluids in skewed plate sandwich structures to find the critical condition leading to the instability of the structure. Moreover, they compared the numerical results obtained by finite element analysis to those of sandwich structures with viscoelastic cores. A comprehensive study, on the influence of different parameters, was also given showing the significant effect of the electrical field on the vibrational behavior of skewed plates. Tabassian and Rezaeepazhand [30] investigated the effects of ER fluid cores on the dynamic stability of sandwich beams under different axial loadings. The beam was constructed using cross-ply composite layers. They concluded that besides the geometrical properties and composite layers configuration, applying the electrical field to the ER fluid core had a considerable effect on improving the stability of the structure under axial loading for different boundary conditions. This kind of system can be used in many structures such as Refs. [31–33]. Gavin et al. [34] employed a numerical method to investigate the flow of ER fluid in rectangular ducts. Since the ER fluid properties could change almost immediately (within thousandths of a second) after applying an electrical field, they are extremely useful in controlling fluid flow in rectangular ducts and other annular duct shapes. Yeh and Chen [35] studied the effects of fluid cores on the vibration of sandwich plates under axial forces. The natural frequencies of this structure were obtained under different applied electrical fields. It was concluded that ER core could effectively reduce the instability region of the structure, Gholamzadeh Babaki [36]. The stability of nano-structures, made from graphene nanoplatelets' reinforced composites and magnetorheological fluids, was investigated by Liuet al. [37]. They considered several parameters including magnetic field in their analysis to observe the stability condition of a cylindrical structure. In the mentioned article, a novel

approach using an artificial intelligence method was utilized to bypass the complexity of derivation and solving equations of motion in such small-scale structures.

Using scale-dependent theories is inevitable in nano- and micro-scale structures. In these structures, due to small-scale effects, the responses of fluids and solids are significantly different from macro-scale ones. Thus, conventional theories could not be appropriately implemented on these small scales [38]. Theories similar to nonlocal strain gradient [39], nonlocal elasticity, modified coupled stress [40,41], strain gradient, and some combinations of such theories have been widely used in small scales for dynamic and static analyses.

Ghayesh et al. [42] presented the nonlinear forced dynamics of a three-layered microplate taking into account all the in-plane and out-of-plane motions.

Abzid [43] utilized the nonlocal strain gradient theory (NSGT) to investigate thermal instability, wave propagation, and frequency analysis of small-scale plates. The plate was placed on an elastic substrate and shear deformation plate theory was utilized to observe the effects of magnetic fields on the hygrothermal environment on the buckling and dynamic instability of the structure. Ebrahimi et al. [44] utilized NSGT to investigate wave propagation of functionally graded small-scale plated under nonlinear thermal loading. They considered the effects of several parameters in their study including length-scale effects and geometrical variations of the structure. The porosity of functionally graded nanoplates with piezoelectric patches was investigated by Karami and Shahsavari [45] under thermal loading. Effects of porosity and humidity in hygrothermal material were carefully examined and reported in their study. Vibrational instability of three-dimensional functionally graded nanoplates under harmonic loadings was reported by Karami et al. [46] using NSGT. They put their effort to present a detailed formulation of 3D plates using the Bi-Helmholtz theory.

Solution methods on the complicated equations of length-dependent structures are widespread from analytical solution [47–49] to semi-analytical to purely numerical [50–54] procedures based on the degree of solvability of the equation. While most of the governing equations are preferred to be extracted using energy methods, there are several approaches to solving them. In this regard, KOrayem and Homayooni [55] utilized a semi-analytical approach of generalized differential quadrature rule (GDQR) to solve the modified nonlocal stress theory equation of vibrating micro-sized plates. The method is capable of incorporating different boundary conditions of the plate. Li et al. [56] analyzed wave dispersion in functionally graded plates using NURBS to parameterize the deformed curves. Shi et al. [57] utilized an analytical solution for simply supported small-scale plates made of nano-composites functionally graded materials and a semi-analytical differential quadrature method for other boundary conditions. The nano-plate was modeled using modified couple stress theory and involved a fluid-conveying porous structure. Xu et al. [58] also semi-analytical GDQM to solve the vibration problem of small-scale beams under nonlinear forced vibrations.

Beams are common structural elements in most structures and they are analyzed using classical or refined shear deformation theories to evaluate static and dynamic characteristics. The elementary theory of beam bending underestimate deflections and overestimates the natural frequencies since it disregards the transverse shear deformation effect [59,60].

There are a lot of theories that are used for the analysis of beams [61,62]. The first one is the Euler-Bernoulli theory [63] a classical beam theory that is presented for the analysis of thin beams. In the classical theory of beam, it is assumed that stresses within the thickness

are constant. So, due to this assumption, the theories of the classical beam cannot present precise results for thick and moderate thick beams. The first-order shear deformation theory (FSDT) was presented by Timoshenko [64] to compensate for defects of the classical theory. This theory is now widely referred to as the Timoshenko beam theory or the first-order shear deformation theory. In this theory, transverse shear strain distribution is assumed to be constant through the beam thickness and thus requires a problem-dependent shear correction factor. The accuracy of the Timoshenko beam theory for transverse vibrations of a simply supported beam in respect of the fundamental frequency is verified by Cowper [65] with a plane stress exact elasticity solution. Dynamic stability analysis of an imperfect microscale beam, considering the Timoshenko beam theory and Galerkin's method, was presented by Ref. [66,67].

Khaniki et al. [68] studied time-dependent mechanics of multilayered thick hyperelastic beams using five different types of shear deformation models for modeling the beam (i.e. the Euler–Bernoulli, Timoshenko, third-order, trigonometric, and exponential shear deformable models), and the von Kármán geometrical nonlinearity and Mooney–Rivlin hyperelastic strain energy density.

Artificial intelligence (AI) methods have been the center of attention in recent decades as a promising method replacing complicated numerical and analytical methods [69,70]. In this methodology, the factors affecting the mechanical behaviors of a structure are directly related to outputs using a regression-based analysis. In doing so, extremely nonlinear models are easily modeled with a high accuracy level. On the other hand, using AI models is a simple task to incorporate other parameters in the models without the necessity of deriving and solving all equations. Furthermore, the user of such networks can change the input factors to observe their influence on the output without solving all the equations multiple times. Indeed, once the AI model has been trained, it can predict the outputs based on given inputs. However, the whole efficacy of the AI is dependent on the training process and reliability of provided data during training, validating, and testing of the AI model. The reliable data are provided mainly using experimental data. However, in many cases, the data come from validated numerical simulations.

In the present study, for the first time, the effects of using an electrical field in improving the dynamic stability of nanostructure containing ER fluids are presented. In this regard, a cylindrical sandwich structure with an inner and an outer layer composed of two-directional functionally graded (2D-FG) material and ER fluid core is considered. Employing energy methods and modified power law the equations of motion of the structure are derived. Between FG and ER layers' compatibility conditions are imposed in terms of displacement and strains. Moreover, to bypass computational complications, the inputs and outputs are utilized for training the DNN. In this way, the inputs and outputs are related to each other through the regression method without numerically solving the equations of motion all over again. Finally, the effects of different parameters on the vibrational characteristics of the structure will be presented.

2. Equivalent material properties

The geometry of the cylindrical composite structure is depicted in Figure 1. The cylinder is composed of 3 layers. The inner and outer layers are FG material which are graded in two directions. The core layer is ER fluid. The inner radius of the structure is R_i , the outer radius

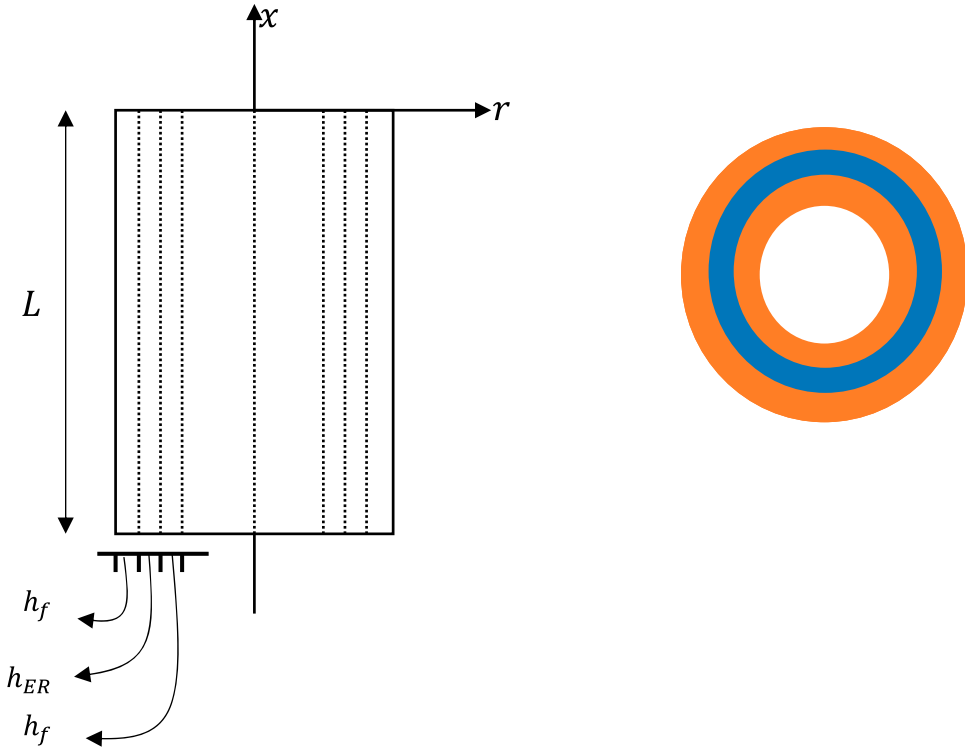


Figure 1. Illustration of the composite nano pipe structure.

is R_o , the thickness of FG layers is equal to h_f , and the thickness of the core layer is h_{ER} . Moreover, the total thickness of the hollow cylinder is $h = h_{ER} + 2h_f$.

2.1. Material characteristics for FG layers

According to the modified power law, the graded property P of the FG layers is expressed using the following relation:

$$P(x, z) = P_m + (P_c - P_m)e^{\frac{n_x x}{L} + n_z(0.5 + \frac{z}{h})} \quad (1)$$

where P represents any of elastic constants and mass density of the FG material. Moreover, the indices n_x and n_z represent the grading index of the FG layers in radial and axial directions, respectively. As in the FG layers the mid-surface differs from the neutral surface [71], in this study we also follow it.

2.2. ER fluid core

The complex shear modulus G^* of an ER fluid is composed of two separate parts, representing pre – and post-yield regimes. For a linear viscoelastic ER fluid, the relation between shear stress and shear strain is as follows:

$$\tau = \mathbf{G}^* \gamma \rightarrow \begin{cases} \tau_{xzc} = G^* \gamma_{xzc} \\ \tau_{yzc} = G^* \gamma_{yzc} \end{cases} \quad (2)$$

where τ and γ represent the shear stress and strain tensors, respectively. G^* is a complex quantity and is decomposed into real and imaginary parts as shown below:

$$G^* = G' + iG'' \text{ or } G^* = G'(1 + i\eta) \quad (3)$$

where $\eta = \frac{G''}{G'}$ is the loss factor and $i = \sqrt{-1}$ is the imaginary unit. The modulus G' is proportional to the stored energy in ER fluid and called the storage modulus, while the modulus G'' is the dissipation part and it is proportional to the energy loss in each cycle of deformation of the ER fluid.

The post-yield behavior of ER fluid is characterized by the following relation between shear stress and strain:

$$\tau = \tau_y + \mu\dot{\gamma} \quad (4)$$

where τ_y is the initial yield strength induced by the electrical field and the parameter μ is the flow viscosity. The time derivative of shear strain $\dot{\gamma}$ is the shear rate in the post-yield regime. In addition, it is assumed:

- FG layers are completely bonded to the ER core.
- There is no compression or stretch in the thickness direction.
- The elasticity modulus of the ER fluid is negligible in comparison to the FG material.

3. Displacement fields

The core ER fluid material is modeled as the higher-order shear deformation theory (HSDT) [72,73] and the FG face sheets are modeled using the first-order shear deformation theory (FSDT) as below:

$$\begin{aligned} u_c(r, z, t) &= u_{0c}(z, t) + ru_{1c}(z, t) + r^2u_{2c}(z, t) + r^3u_{3c}(z, t) \\ v_c(r, z, t) &= 0 \\ w_c(r, z, t) &= w_{0c}(z, t) + rw_{1c}(z, t) + r^2w_{2c}(z, t) + r^3w_{3c}(z, t) \\ u_b(r, z, t) &= u_{0b}(z, t) + ru_{1b}(z, t) \\ v_b(r, z, t) &= v_{0b}(z, t) + rv_{1b}(z, t) \\ w_b(r, z, t) &= w_{0b}(z, t) \\ u_t(r, z, t) &= u_{0t}(z, t) + ru_{1t}(z, t) \\ v_t(r, z, t) &= v_{0t}(z, t) + rv_{1t}(z, t) \\ w_t(r, z, t) &= w_{0t}(z, t) \end{aligned} \quad (5)$$

where u_0 , v_0 , and w_0 are the functions of time and axial coordinate z , and thickness direction r . Other functions u_{1i} , u_{2i} , u_{3i} , w_{1c} , w_{2c} , w_{3c} , and v_{1i} are functions of the rotation about normal to the middle surface.

3.1. Compatibility conditions

In the interface of the FG layers and the core the following displacement constraints are imposed for fully bonding the layers:

$$\begin{aligned}
 u_t \left(x, \frac{h_c}{2}, t \right) &= u_c \left(x, \frac{h_c}{2}, t \right) \\
 v_t \left(x, \frac{h_c}{2}, t \right) &= v_c \left(x, \frac{h_c}{2}, t \right) \\
 w_t \left(x, \frac{h_c}{2}, t \right) &= w_c \left(x, \frac{h_c}{2}, t \right) \\
 u_b \left(x, -\frac{h_c}{2}, t \right) &= u_c \left(x, -\frac{h_c}{2}, t \right) \\
 v_b \left(x, -\frac{h_c}{2}, t \right) &= v_c \left(x, -\frac{h_c}{2}, t \right) \\
 w_b \left(x, -\frac{h_c}{2}, t \right) &= w_c \left(x, -\frac{h_c}{2}, t \right)
 \end{aligned} \tag{6}$$

Using Eqs. (5) and (6) the displacement field could be written in the following form:

$$\begin{aligned}
 u_t(x, z, t) &= u_{0c}(x, \theta) + (R_o - h_{GPL})u_{1c}(x, \theta) + (z - (R_o - h_{GPL}))u_{1t}(x, \theta) \\
 v_t(x, z, t) &= v_{0c}(x, \theta) + (R_o - h_{GPL})v_{1c}(x, \theta) + (z - (R_o - h_{GPL}))v_{1t}(x, \theta) \\
 w_t(x, \theta, z) &= w_{0c}(x, \theta) \\
 u_b(x, z, t) &= u_{0c}(x, \theta) + (R_i + h_{GPL})u_{1c}(x, \theta) + (z - (R_i + h_{GPL}))u_{1b}(x, \theta) \\
 v_b(x, z, t) &= v_{0c}(x, \theta) + (R_i + h_{GPL})v_{1c}(x, \theta) + (z - (R_i + h_{GPL}))v_{1b}(x, \theta) \\
 w_b(x, z, t) &= w_{0c}(x, \theta) \\
 u_c(x, z, t) &= u_{0c}(x, \theta) + zu_{1c}(x, \theta) \\
 v_c(x, z, t) &= v_{0c}(x, \theta) + zv_{1c}(x, \theta) \\
 w_c(x, z, t) &= w_{0c}(x, \theta)
 \end{aligned} \tag{7}$$

The relation between ER fluid in the core layer is as below:

$$\begin{aligned}
 \sigma_{xxc} &= Q_{11c}\varepsilon_{xxc} + Q_{13c}\varepsilon_{zzc} \\
 \sigma_{zzc} &= Q_{13c}\varepsilon_{xxc} + Q_{33c}\varepsilon_{zzc} \\
 \tau_{xzc} &= Q_{55c}\gamma_{xzc}
 \end{aligned} \tag{8}$$

in which [74–78]

$$Q_{11c} = Q_{22c} = 0, Q_{12c} = 0, Q_{44c} = Q_{66c} = 0, Q_{55c} = G^* \tag{9}$$

The FG layers are considered to be elastic material with small deformation so the stress and strain relation could be given by the following relations:

$$\sigma_{xxj} = Q_{11j}\varepsilon_{xxj} + Q_{13j}\varepsilon_{zzj}$$

$$\begin{aligned}\sigma_{zzj} &= Q_{13j}\varepsilon_{xxj} + Q_{33j}\varepsilon_{zzj} \\ \tau_{xzt} &= Q_{55j}\gamma_{xzt}\end{aligned}\quad (10)$$

in which [79–82]

$$Q_{11j} = \frac{E_c}{1 - \nu_c^2}, Q_{33j} = \frac{E_c}{1 - \nu_c^2}, Q_{13j} = \frac{\nu E_c}{1 - \nu_c^2}, Q_{55j} = G_c \quad (11)$$

here $j = b, t$. Moreover, the strain components are calculated using the following relations using displacement components:

$$\begin{aligned}\varepsilon_{xx} &= \frac{\partial u}{\partial x} \\ \varepsilon_{zz} &= \frac{\partial w}{\partial z} \\ \gamma_{xz} &= \frac{\partial u}{\partial z} + \frac{\partial w}{\partial x}\end{aligned}\quad (12)$$

3.2. Minimizing virtual work and equations of motion

The virtual work of the structure could be minimized by setting its variation equal to zero. The following relation is called Hamilton's principle [83–86]:

$$\int_{t_1}^{t_2} (\delta \Pi_k - \delta \Pi_e) dt = 0 \quad (13)$$

Internal energy and kinetic energy of the structures are represented by Π_e and Π_k which are expressed as the following relations [87–89]:

$$\Pi_k = \int \left[\begin{aligned} &\rho \left\{ \left(\frac{\partial u_t}{\partial t} \right)^2 + \left(\frac{\partial v_t}{\partial t} \right)^2 + \left(\frac{\partial w_t}{\partial t} \right)^2 \right\} \\ &+ \rho \left\{ \left(\frac{\partial u_c}{\partial t} \right)^2 + \left(\frac{\partial v_c}{\partial t} \right)^2 + \left(\frac{\partial w_c}{\partial t} \right)^2 \right\} \\ &+ \rho \left\{ \left(\frac{\partial u_b}{\partial t} \right)^2 + \left(\frac{\partial v_b}{\partial t} \right)^2 + \left(\frac{\partial w_b}{\partial t} \right)^2 \right\} \end{aligned} \right] dV \quad (14a)$$

$$\Pi_e = \int \{ \sigma_{xxt}\varepsilon_{xxt} + \sigma_{zzt}\varepsilon_{zzt} + \tau_{xzt}\gamma_{xzt} + \sigma_{xxb}\varepsilon_{xxb} + \sigma_{zzb}\varepsilon_{zzb} + \tau_{xzb}\gamma_{xzb} + \tau_{xzc}\gamma_{xzc} \} dV \quad (14b)$$

Substituting the above relation into Eq. (13), performing part by part integral and equating all the variations coefficients to zero, the following set of equations will be obtained:

$$\begin{aligned}\delta u_{1b} : & \frac{\partial M_{xxb}}{\partial x} + \frac{h_c}{2} \frac{\partial N_{xxb}}{\partial x} - N_{xzb} \\ &= \left(\begin{aligned} &l_{1b} \frac{\partial^2 u_{0c}}{\partial t^2} + l_{2b} \frac{\partial^2 u_{1b}}{\partial t^2} + \frac{h_c}{2} l_{1b} \frac{\partial^2 u_{1b}}{\partial t^2} - \frac{h_c}{2} l_{1b} \frac{\partial^2 u_{1c}}{\partial t^2} \\ &+ \left(\frac{h_c}{2} \right)^2 l_{1b} \frac{\partial^2 u_{2c}}{\partial t^2} - \left(\frac{h_c}{2} \right)^3 l_{1b} \frac{\partial^2 u_{3c}}{\partial t^2} \end{aligned} \right)\end{aligned}$$

$$\begin{aligned}
& + \frac{h_c}{2} \left(l_{0b} \frac{\partial^2 u_{0c}}{\partial t^2} + l_{1b} \frac{\partial^2 u_{1b}}{\partial t^2} + \frac{h_c}{2} l_{0b} \frac{\partial^2 u_{1b}}{\partial t^2} - \frac{h_c}{2} l_{0b} \frac{\partial^2 u_{1c}}{\partial t^2} \right. \\
& \quad \left. + \left(\frac{h_c}{2} \right)^2 l_{0b} \frac{\partial^2 u_{2c}}{\partial t^2} - \left(\frac{h_c}{2} \right)^3 l_{0b} \frac{\partial^2 u_{3c}}{\partial t^2} \right) \\
\delta u_{0c} : & \frac{\partial N_{xxb}}{\partial x} + \frac{\partial N_{xxt}}{\partial x} \\
& = \left(l_{0b} \frac{\partial^2 u_{0c}}{\partial t^2} + l_{1b} \frac{\partial^2 u_{1b}}{\partial t^2} + \frac{h_c}{2} l_{0b} \frac{\partial^2 u_{1b}}{\partial t^2} - \frac{h_c}{2} l_{0b} \frac{\partial^2 u_{1c}}{\partial t^2} \right. \\
& \quad \left. + \left(\frac{h_c}{2} \right)^2 l_{0b} \frac{\partial^2 u_{2c}}{\partial t^2} - \left(\frac{h_c}{2} \right)^3 l_{0b} \frac{\partial^2 u_{3c}}{\partial t^2} \right) \\
& \quad + \left(l_{0c} \frac{\partial^2 u_{0c}}{\partial t^2} + l_{1c} \frac{\partial^2 u_{1c}}{\partial t^2} + l_{2c} \frac{\partial^2 u_{2c}}{\partial t^2} + l_{3c} \frac{\partial^2 u_{3c}}{\partial t^2} \right) \\
& \quad + \left(l_{0t} \frac{\partial^2 u_{0c}}{\partial t^2} + l_{1t} \frac{\partial^2 u_{1t}}{\partial t^2} - \frac{h_c}{2} l_{0t} \frac{\partial^2 u_{1t}}{\partial t^2} + \frac{h_c}{2} l_{0t} \frac{\partial^2 u_{1c}}{\partial t^2} \right. \\
& \quad \left. + \left(\frac{h_c}{2} \right)^2 l_{0t} \frac{\partial^2 u_{2c}}{\partial t^2} + \left(\frac{h_c}{2} \right)^3 l_{0t} \frac{\partial^2 u_{3c}}{\partial t^2} \right) \\
\delta w_{0c} : & \frac{\partial N_{xzb}}{\partial x} + \frac{\partial N_{xzt}}{\partial x} + \frac{\partial N_{xzc}}{\partial x} \\
& = \left(l_{0b} \frac{\partial^2 w_{0c}}{\partial t^2} - \frac{h_c}{2} l_{0b} \frac{\partial^2 w_{1c}}{\partial t^2} + \left(\frac{h_c}{2} \right)^2 l_{0b} \frac{\partial^2 w_{2c}}{\partial t^2} - \left(\frac{h_c}{2} \right)^3 l_{0b} \frac{\partial^2 w_{3c}}{\partial t^2} \right) \\
& \quad + \left(l_{0c} \frac{\partial^2 w_{0c}}{\partial t^2} + l_{1c} \frac{\partial^2 w_{1c}}{\partial t^2} + l_{2c} \frac{\partial^2 w_{2c}}{\partial t^2} + l_{3c} \frac{\partial^2 w_{3c}}{\partial t^2} \right) \\
& \quad + \left(l_{0t} \frac{\partial^2 w_{0c}}{\partial t^2} + \frac{h_c}{2} l_{0t} \frac{\partial^2 w_{1c}}{\partial t^2} + \left(\frac{h_c}{2} \right)^2 l_{0t} \frac{\partial^2 w_{2c}}{\partial t^2} + \left(\frac{h_c}{2} \right)^3 l_{0t} \frac{\partial^2 w_{3c}}{\partial t^2} \right) \\
\delta u_{1c} : & -\frac{h_c}{2} \frac{\partial N_{xxb}}{\partial x} + \frac{h_c}{2} \frac{\partial N_{xxt}}{\partial x} - N_{xzc} = \\
& \quad - \frac{h_c}{2} \left(l_{0b} \frac{\partial^2 u_{0c}}{\partial t^2} + l_{1b} \frac{\partial^2 u_{1b}}{\partial t^2} + \frac{h_c}{2} l_{0b} \frac{\partial^2 u_{1b}}{\partial t^2} - \frac{h_c}{2} l_{0b} \frac{\partial^2 u_{1c}}{\partial t^2} \right. \\
& \quad \left. + \left(\frac{h_c}{2} \right)^2 l_{0b} \frac{\partial^2 u_{2c}}{\partial t^2} - \left(\frac{h_c}{2} \right)^3 l_{0b} \frac{\partial^2 u_{3c}}{\partial t^2} \right) \\
& \quad + \left(l_{1c} \frac{\partial^2 u_{0c}}{\partial t^2} + l_{2c} \frac{\partial^2 u_{1c}}{\partial t^2} + l_{3c} \frac{\partial^2 u_{2c}}{\partial t^2} + l_{4c} \frac{\partial^2 u_{3c}}{\partial t^2} \right) \\
& \quad + \frac{h_c}{2} \left(l_{0t} \frac{\partial^2 u_{0c}}{\partial t^2} + l_{1t} \frac{\partial^2 u_{1t}}{\partial t^2} - \frac{h_c}{2} l_{0t} \frac{\partial^2 u_{1t}}{\partial t^2} + \frac{h_c}{2} l_{0t} \frac{\partial^2 u_{1c}}{\partial t^2} \right. \\
& \quad \left. + \left(\frac{h_c}{2} \right)^2 l_{0t} \frac{\partial^2 u_{2c}}{\partial t^2} + \left(\frac{h_c}{2} \right)^3 l_{0t} \frac{\partial^2 u_{3c}}{\partial t^2} \right) \\
\delta w_{1c} : & -\frac{h_c}{2} \frac{\partial N_{xzb}}{\partial x} + \frac{h_c}{2} \frac{\partial N_{xzt}}{\partial x} + \frac{\partial M_{xzc}}{\partial x} =
\end{aligned}$$

$$\begin{aligned}
& -\frac{h_c}{2} \left(l_{0b} \frac{\partial^2 w_{0c}}{\partial t^2} - \frac{h_c}{2} l_{0b} \frac{\partial^2 w_{1c}}{\partial t^2} + \left(\frac{h_c}{2} \right)^2 l_{0b} \frac{\partial^2 w_{2c}}{\partial t^2} - \left(\frac{h_c}{2} \right)^3 l_{0b} \frac{\partial^2 w_{3c}}{\partial t^2} \right) \\
& + \left(l_{1c} \frac{\partial^2 w_{0c}}{\partial t^2} + l_{2c} \frac{\partial^2 w_{1c}}{\partial t^2} + l_{3c} \frac{\partial^2 w_{2c}}{\partial t^2} + l_{4c} \frac{\partial^2 w_{3c}}{\partial t^2} \right) \\
& + \frac{h_c}{2} \left(l_{0t} \frac{\partial^2 w_{0c}}{\partial t^2} + \frac{h_c}{2} l_{0t} \frac{\partial^2 w_{1c}}{\partial t^2} + \left(\frac{h_c}{2} \right)^2 l_{0t} \frac{\partial^2 w_{2c}}{\partial t^2} + \left(\frac{h_c}{2} \right)^3 l_{0t} \frac{\partial^2 w_{3c}}{\partial t^2} \right) \\
\delta u_{2c} : & - \left(\frac{h_c}{2} \right)^2 \frac{\partial N_{xxb}}{\partial x} + \left(\frac{h_c}{2} \right)^2 \frac{\partial N_{xxt}}{\partial x} - 2M_{xzc} \\
& = \left(\frac{h_c}{2} \right)^2 \left(l_{0b} \frac{\partial^2 u_{0c}}{\partial t^2} + l_{1b} \frac{\partial^2 u_{1b}}{\partial t^2} + \frac{h_c}{2} l_{0b} \frac{\partial^2 u_{1b}}{\partial t^2} \right. \\
& \quad \left. - \frac{h_c}{2} l_{0b} \frac{\partial^2 u_{1c}}{\partial t^2} + \left(\frac{h_c}{2} \right)^2 l_{0b} \frac{\partial^2 u_{2c}}{\partial t^2} - \left(\frac{h_c}{2} \right)^3 l_{0b} \frac{\partial^2 u_{3c}}{\partial t^2} \right) \\
& + \left(l_{2c} \frac{\partial^2 u_{0c}}{\partial t^2} + l_{3c} \frac{\partial^2 u_{1c}}{\partial t^2} + l_{4c} \frac{\partial^2 u_{2c}}{\partial t^2} + l_{5c} \frac{\partial^2 u_{3c}}{\partial t^2} \right) \\
& + \left(\frac{h_c}{2} \right)^2 \left(l_{0t} \frac{\partial^2 u_{0c}}{\partial t^2} + l_{1t} \frac{\partial^2 u_{1t}}{\partial t^2} - \frac{h_c}{2} l_{0t} \frac{\partial^2 u_{1t}}{\partial t^2} + \frac{h_c}{2} l_{0t} \frac{\partial^2 u_{1c}}{\partial t^2} \right. \\
& \quad \left. + \left(\frac{h_c}{2} \right)^2 l_{0t} \frac{\partial^2 u_{2c}}{\partial t^2} + \left(\frac{h_c}{2} \right)^3 l_{0t} \frac{\partial^2 u_{3c}}{\partial t^2} \right) \\
\delta w_{2c} : & - \left(\frac{h_c}{2} \right)^2 \frac{\partial N_{xzb}}{\partial x} + \left(\frac{h_c}{2} \right)^2 \frac{\partial N_{xzt}}{\partial x} + \frac{\partial P_{xzc}}{\partial x} = \\
& + \left(\frac{h_c}{2} \right)^2 \left(l_{0b} \frac{\partial^2 w_{0c}}{\partial t^2} - \frac{h_c}{2} l_{0b} \frac{\partial^2 w_{1c}}{\partial t^2} + \left(\frac{h_c}{2} \right)^2 l_{0b} \frac{\partial^2 w_{2c}}{\partial t^2} - \left(\frac{h_c}{2} \right)^3 l_{0b} \frac{\partial^2 w_{3c}}{\partial t^2} \right) \\
& + \left(l_{2c} \frac{\partial^2 w_{0c}}{\partial t^2} + l_{3c} \frac{\partial^2 w_{1c}}{\partial t^2} + l_{4c} \frac{\partial^2 w_{2c}}{\partial t^2} + l_{5c} \frac{\partial^2 w_{3c}}{\partial t^2} \right) \\
& + \left(\frac{h_c}{2} \right)^2 \left(l_{0t} \frac{\partial^2 w_{0c}}{\partial t^2} + \frac{h_c}{2} l_{0t} \frac{\partial^2 w_{1c}}{\partial t^2} + \left(\frac{h_c}{2} \right)^2 l_{0t} \frac{\partial^2 w_{2c}}{\partial t^2} + \left(\frac{h_c}{2} \right)^3 l_{0t} \frac{\partial^2 w_{3c}}{\partial t^2} \right) \\
\delta u_{3c} : & - \left(\frac{h_c}{2} \right)^3 \frac{\partial N_{xxb}}{\partial x} + \left(\frac{h_c}{2} \right)^3 \frac{\partial N_{xxt}}{\partial x} - 3P_{xzc} = \\
& - \left(\frac{h_c}{2} \right)^3 \left(l_{0b} \frac{\partial^2 u_{0c}}{\partial t^2} + l_{1b} \frac{\partial^2 u_{1b}}{\partial t^2} + \frac{h_c}{2} l_{0b} \frac{\partial^2 u_{1b}}{\partial t^2} \right. \\
& \quad \left. - \frac{h_c}{2} l_{0b} \frac{\partial^2 u_{1c}}{\partial t^2} + \left(\frac{h_c}{2} \right)^2 l_{0b} \frac{\partial^2 u_{2c}}{\partial t^2} - \left(\frac{h_c}{2} \right)^3 l_{0b} \frac{\partial^2 u_{3c}}{\partial t^2} \right) \\
& + \left(l_{3c} \frac{\partial^2 u_{0c}}{\partial t^2} + l_{4c} \frac{\partial^2 u_{1c}}{\partial t^2} + l_{5c} \frac{\partial^2 u_{2c}}{\partial t^2} + l_{6c} \frac{\partial^2 u_{3c}}{\partial t^2} \right)
\end{aligned}$$

$$\begin{aligned}
& + \left(\frac{h_c}{2}\right)^3 \left(l_{0t} \frac{\partial^2 u_{0c}}{\partial t^2} + l_{1t} \frac{\partial^2 u_{1t}}{\partial t^2} - \frac{h_c}{2} l_{0t} \frac{\partial^2 u_{1t}}{\partial t^2} + \frac{h_c}{2} l_{0t} \frac{\partial^2 u_{1c}}{\partial t^2} \right. \\
& \quad \left. + \left(\frac{h_c}{2}\right)^2 l_{0t} \frac{\partial^2 u_{2c}}{\partial t^2} + \left(\frac{h_c}{2}\right)^3 l_{0t} \frac{\partial^2 u_{3c}}{\partial t^2} \right) \\
\delta w_{3c} : & - \left(\frac{h_c}{2}\right)^3 \frac{\partial N_{xzb}}{\partial x} + \left(\frac{h_c}{2}\right)^3 \frac{\partial N_{xzt}}{\partial x} + \frac{\partial Q_{xzc}}{\partial x} = \\
& - \left(\frac{h_c}{2}\right)^3 \left(l_{0b} \frac{\partial^2 w_{0c}}{\partial t^2} - \frac{h_c}{2} l_{0b} \frac{\partial^2 w_{1c}}{\partial t^2} + \left(\frac{h_c}{2}\right)^2 l_{0b} \frac{\partial^2 w_{2c}}{\partial t^2} - \left(\frac{h_c}{2}\right)^3 l_{0b} \frac{\partial^2 w_{3c}}{\partial t^2} \right) \\
& + \left(l_{3c} \frac{\partial^2 w_{0c}}{\partial t^2} + l_{4c} \frac{\partial^2 w_{1c}}{\partial t^2} + l_{5c} \frac{\partial^2 w_{2c}}{\partial t^2} + l_{6c} \frac{\partial^2 w_{3c}}{\partial t^2} \right) \\
& + \left(\frac{h_c}{2}\right)^3 \left(l_{0t} \frac{\partial^2 w_{0c}}{\partial t^2} + \frac{h_c}{2} l_{0t} \frac{\partial^2 w_{1c}}{\partial t^2} + \left(\frac{h_c}{2}\right)^2 l_{0t} \frac{\partial^2 w_{2c}}{\partial t^2} + \left(\frac{h_c}{2}\right)^3 l_{0t} \frac{\partial^2 w_{3c}}{\partial t^2} \right) \\
\delta u_{1t} : & \frac{\partial M_{xxt}}{\partial x} - \frac{h_c}{2} \frac{\partial N_{xxt}}{\partial x} - N_{xzt} \\
& = \left(l_{1t} \frac{\partial^2 u_{0c}}{\partial t^2} + l_{2t} \frac{\partial^2 u_{1t}}{\partial t^2} - \frac{h_c}{2} l_{1t} \frac{\partial^2 u_{1t}}{\partial t^2} + \frac{h_c}{2} l_{1t} \frac{\partial^2 u_{1c}}{\partial t^2} \right. \\
& \quad \left. + \left(\frac{h_c}{2}\right)^2 l_{1t} \frac{\partial^2 u_{2c}}{\partial t^2} + \left(\frac{h_c}{2}\right)^3 l_{1t} \frac{\partial^2 u_{3c}}{\partial t^2} \right) \\
& + \frac{h_c}{2} \left(l_{0t} \frac{\partial^2 u_{0c}}{\partial t^2} + l_{1t} \frac{\partial^2 u_{1t}}{\partial t^2} - \frac{h_c}{2} l_{0t} \frac{\partial^2 u_{1t}}{\partial t^2} + \frac{h_c}{2} l_{0t} \frac{\partial^2 u_{1c}}{\partial t^2} \right. \\
& \quad \left. + \left(\frac{h_c}{2}\right)^2 l_{0t} \frac{\partial^2 u_{2c}}{\partial t^2} + \left(\frac{h_c}{2}\right)^3 l_{0t} \frac{\partial^2 u_{3c}}{\partial t^2} \right) \tag{15}
\end{aligned}$$

where

$$\begin{aligned}
\{N_{xxt}, M_{xxt}\} &= \int \{1, z\} \sigma_{xxt} dz, \quad \{N_{xxb}, M_{xxb}\} = \int \{1, z\} \sigma_{xxb} dz, \\
\{N_{zzt}, M_{zzt}\} &= \int \{1, z\} \sigma_{zzt} dz, \quad \{N_{zzb}, M_{zzb}\} = \int \{1, z\} \sigma_{zzb} dz, \{N_{xzt}, M_{xzt}\} \\
&= \int \{1, z\} \tau_{xzt} dz, \quad \{N_{xzb}, M_{xzb}\} = \int \{1, z\} \tau_{xzb} dz, \\
\{N_{xzc}, M_{xzc}, P_{xzc}, Q_{xzc}\} &= \int \{1, z, z^2, z^3\} \tau_{xzc} dz \\
\{l_{0b}, l_{1b}, l_{2b}\} &= \int \{1, z, z^2\} \rho dz, \quad \{l_{0t}, l_{1t}, l_{2t}\} = \int \{1, z, z^2\} \rho dz, \\
\{l_{0c}, l_{1c}, l_{2c}, l_{3c}, l_{4c}, l_{5c}, l_{6c}\} &= \int \{1, z, z^2, z^3, z^4, z^5, z^6\} \rho dz \tag{16}
\end{aligned}$$

Moreover, from the same variational integral, the following natural boundary conditions are obtained:

$$\delta u_{1t} : \quad P_{xxt} \hat{n}_x + \left(\frac{P_{x\theta t}}{R} \right) \hat{n}_\theta = 0$$

$$\begin{aligned}
\delta v_{1t} : \quad & P_{x\theta t} \hat{n}_x + \left(\frac{P_{\theta\theta t}}{R} \right) \hat{n}_\theta = 0 \\
\delta u_{0c} : \quad & (N_{xxt} + N_{xxb}) \hat{n}_x + \left(\frac{N_{x\theta t}}{R} + \frac{N_{x\theta b}}{R} \right) \hat{n}_\theta = 0 \\
\delta v_{0c} : \quad & (N_{x\theta t} + N_{x\theta b}) \hat{n}_x + \left(\frac{N_{\theta\theta t}}{R} + \frac{N_{\theta\theta b}}{R} \right) \hat{n}_\theta = 0 \\
\delta w_{0c} : \quad & (N_{xzt} + N_{xzc} + N_{xzb}) \hat{n}_x + \left(\frac{N_{\theta zt}}{R} + \frac{N_{\theta zc}}{R} + \frac{N_{\theta zb}}{R} \right) \hat{n}_\theta = 0 \\
\delta u_{1c} : \quad & (M_{xxb} + M_{xxt}) \hat{n}_x + \left(\frac{M_{x\theta b}}{R} + \frac{M_{x\theta t}}{R} \right) \hat{n}_\theta = 0 \\
\delta v_{1c} : \quad & (M_{x\theta b} + M_{x\theta t}) \hat{n}_x + \left(\frac{M_{\theta\theta b}}{R} + \frac{M_{\theta\theta c}}{R} + \frac{M_{\theta\theta t}}{R} \right) \hat{n}_\theta = 0 \\
\delta u_{1b} : \quad & P_{xxb} \hat{n}_x + \left(\frac{P_{x\theta b}}{R} \right) \hat{n}_\theta = 0 \\
\delta v_{1b} : \quad & P_{x\theta b} \hat{n}_x + \left(\frac{P_{\theta\theta b}}{R} \right) \hat{n}_\theta = 0
\end{aligned} \tag{17}$$

3.3. The nonlocal strain gradient theory

The simplified constitutive equation in the nonlocal strain gradient theory could be expressed as [44]

$$[1 - (ea)^2 \nabla^2] \sigma_{ij} = (1 - l^2 \nabla^2) \sigma_{ij}^c \tag{18}$$

in which the operator ∇^2 is Laplacian which is defined as follows:

$$\nabla^2 = \frac{\partial^2}{\partial x^2} + \frac{\partial^2}{\partial y^2} + \frac{\partial^2}{\partial z^2} \tag{19}$$

Moreover, e is the nonlocal parameter and a is the internal characteristic length. The parameter l is the length scale parameter of the gradient part of the constitutive equation. The tensor σ_{ij} is the actual stress tensor component and σ_{ij}^c the classical stress tensor component which are obtained neglecting nonlocal and gradient effects. Using the stress components presented in Eq. (18) is substituting these stresses into Eq. (16) and later in Eq. (15), the following equations which are purely dependent on the displacement components:

$$\delta u_{1b} : \left(1 - l^2 \frac{\partial^2}{\partial x^2} \right) \left(\frac{\partial M_{xxb}}{\partial x} + \frac{h_c}{2} \frac{\partial N_{xxb}}{\partial x} - N_{xzb} \right)$$

$$\begin{aligned}
&= \left(1 - \mu^2 \frac{\partial^2}{\partial x^2}\right) \left(\begin{aligned} &\left(l_{1b} \frac{\partial^2 u_{0c}}{\partial t^2} + l_{2b} \frac{\partial^2 u_{1b}}{\partial t^2} + \frac{h_c}{2} l_{1b} \frac{\partial^2 u_{1b}}{\partial t^2} - \frac{h_c}{2} l_{1b} \frac{\partial^2 u_{1c}}{\partial t^2} \right) \\ &+ \left(\frac{h_c}{2} \right)^2 l_{1b} \frac{\partial^2 u_{2c}}{\partial t^2} - \left(\frac{h_c}{2} \right)^3 l_{1b} \frac{\partial^2 u_{3c}}{\partial t^2} \\ &+ \frac{h_c}{2} \left(l_{0b} \frac{\partial^2 u_{0c}}{\partial t^2} + l_{1b} \frac{\partial^2 u_{1b}}{\partial t^2} + \frac{h_c}{2} l_{0b} \frac{\partial^2 u_{1b}}{\partial t^2} - \frac{h_c}{2} l_{0b} \frac{\partial^2 u_{1c}}{\partial t^2} \right) \\ &+ \left(\frac{h_c}{2} \right)^2 l_{0b} \frac{\partial^2 u_{2c}}{\partial t^2} - \left(\frac{h_c}{2} \right)^3 l_{0b} \frac{\partial^2 u_{3c}}{\partial t^2} \end{aligned} \right) \\
\delta u_{0c} : &\left(1 - \mu^2 \frac{\partial^2}{\partial x^2}\right) \left(\frac{\partial N_{xxb}}{\partial x} + \frac{\partial N_{xxt}}{\partial x} \right) \\
&= \left(1 - \mu^2 \frac{\partial^2}{\partial x^2}\right) \left(\begin{aligned} &\left(l_{0b} \frac{\partial^2 u_{0c}}{\partial t^2} + l_{1b} \frac{\partial^2 u_{1b}}{\partial t^2} + \frac{h_c}{2} l_{0b} \frac{\partial^2 u_{1b}}{\partial t^2} - \frac{h_c}{2} l_{0b} \frac{\partial^2 u_{1c}}{\partial t^2} \right) \\ &+ \left(\frac{h_c}{2} \right)^2 l_{0b} \frac{\partial^2 u_{2c}}{\partial t^2} - \left(\frac{h_c}{2} \right)^3 l_{0b} \frac{\partial^2 u_{3c}}{\partial t^2} \\ &+ \left(l_{0c} \frac{\partial^2 u_{0c}}{\partial t^2} + l_{1c} \frac{\partial^2 u_{1c}}{\partial t^2} + l_{2c} \frac{\partial^2 u_{2c}}{\partial t^2} + l_{3c} \frac{\partial^2 u_{3c}}{\partial t^2} \right) \\ &+ \left(l_{0t} \frac{\partial^2 u_{0c}}{\partial t^2} + l_{1t} \frac{\partial^2 u_{1t}}{\partial t^2} - \frac{h_c}{2} l_{0t} \frac{\partial^2 u_{1t}}{\partial t^2} + \frac{h_c}{2} l_{0t} \frac{\partial^2 u_{1c}}{\partial t^2} \right) \\ &+ \left(\frac{h_c}{2} \right)^2 l_{0t} \frac{\partial^2 u_{2c}}{\partial t^2} + \left(\frac{h_c}{2} \right)^3 l_{0t} \frac{\partial^2 u_{3c}}{\partial t^2} \end{aligned} \right) \\
\delta w_{0c} : &\left(1 - \mu^2 \frac{\partial^2}{\partial x^2}\right) \left(\frac{\partial N_{xzb}}{\partial x} + \frac{\partial N_{xzt}}{\partial x} + \frac{\partial N_{xzc}}{\partial x} \right) \\
&= \left(1 - \mu^2 \frac{\partial^2}{\partial x^2}\right) \\
&\quad \times \left(\begin{aligned} &\left(l_{0b} \frac{\partial^2 w_{0c}}{\partial t^2} - \frac{h_c}{2} l_{0b} \frac{\partial^2 w_{1c}}{\partial t^2} + \left(\frac{h_c}{2} \right)^2 l_{0b} \frac{\partial^2 w_{2c}}{\partial t^2} - \left(\frac{h_c}{2} \right)^3 l_{0b} \frac{\partial^2 w_{3c}}{\partial t^2} \right) \\ &+ \left(l_{0c} \frac{\partial^2 w_{0c}}{\partial t^2} + l_{1c} \frac{\partial^2 w_{1c}}{\partial t^2} + l_{2c} \frac{\partial^2 w_{2c}}{\partial t^2} + l_{3c} \frac{\partial^2 w_{3c}}{\partial t^2} \right) \\ &+ \left(l_{0t} \frac{\partial^2 w_{0c}}{\partial t^2} + \frac{h_c}{2} l_{0t} \frac{\partial^2 w_{1c}}{\partial t^2} + \left(\frac{h_c}{2} \right)^2 l_{0t} \frac{\partial^2 w_{2c}}{\partial t^2} + \left(\frac{h_c}{2} \right)^3 l_{0t} \frac{\partial^2 w_{3c}}{\partial t^2} \right) \end{aligned} \right) \\
\delta u_{1c} : &\left(1 - \mu^2 \frac{\partial^2}{\partial x^2}\right) \left(-\frac{h_c}{2} \frac{\partial N_{xxb}}{\partial x} + \frac{h_c}{2} \frac{\partial N_{xxt}}{\partial x} - N_{xzc} \right)
\end{aligned}$$

$$\begin{aligned}
&= \left(1 - \mu^2 \frac{\partial^2}{\partial x^2}\right) \left(-\frac{h_c}{2} \left(l_{0b} \frac{\partial^2 u_{0c}}{\partial t^2} + l_{1b} \frac{\partial^2 u_{1b}}{\partial t^2} + \frac{h_c}{2} l_{0b} \frac{\partial^2 u_{1b}}{\partial t^2} - \frac{h_c}{2} l_{0b} \frac{\partial^2 u_{1c}}{\partial t^2} \right) \right. \\
&\quad \left. + \left(l_{1c} \frac{\partial^2 u_{0c}}{\partial t^2} + l_{2c} \frac{\partial^2 u_{1c}}{\partial t^2} + l_{3c} \frac{\partial^2 u_{2c}}{\partial t^2} + l_{4c} \frac{\partial^2 u_{3c}}{\partial t^2} \right) \right. \\
&\quad \left. + \frac{h_c}{2} \left(l_{0t} \frac{\partial^2 u_{0c}}{\partial t^2} + l_{1t} \frac{\partial^2 u_{1t}}{\partial t^2} - \frac{h_c}{2} l_{0t} \frac{\partial^2 u_{1t}}{\partial t^2} + \frac{h_c}{2} l_{0t} \frac{\partial^2 u_{1c}}{\partial t^2} \right) \right. \\
&\quad \left. + \left(\frac{h_c}{2} \right)^2 l_{0t} \frac{\partial^2 u_{2c}}{\partial t^2} + \left(\frac{h_c}{2} \right)^3 l_{0t} \frac{\partial^2 u_{3c}}{\partial t^2} \right) \\
\delta w_{1c} : &\left(1 - l^2 \frac{\partial^2}{\partial x^2}\right) \left(-\frac{h_c}{2} \frac{\partial N_{xzb}}{\partial x} + \frac{h_c}{2} \frac{\partial N_{xzt}}{\partial x} + \frac{\partial M_{xzc}}{\partial x} \right) \\
&= \left(1 - \mu^2 \frac{\partial^2}{\partial x^2}\right) \\
&\quad \times \left(-\frac{h_c}{2} \left(l_{0b} \frac{\partial^2 w_{0c}}{\partial t^2} - \frac{h_c}{2} l_{0b} \frac{\partial^2 w_{1c}}{\partial t^2} + \left(\frac{h_c}{2} \right)^2 l_{0b} \frac{\partial^2 w_{2c}}{\partial t^2} - \left(\frac{h_c}{2} \right)^3 l_{0b} \frac{\partial^2 w_{3c}}{\partial t^2} \right) \right. \\
&\quad \left. + \left(l_{1c} \frac{\partial^2 w_{0c}}{\partial t^2} + l_{2c} \frac{\partial^2 w_{1c}}{\partial t^2} + l_{3c} \frac{\partial^2 w_{2c}}{\partial t^2} + l_{4c} \frac{\partial^2 w_{3c}}{\partial t^2} \right) \right. \\
&\quad \left. + \frac{h_c}{2} \left(l_{0t} \frac{\partial^2 w_{0c}}{\partial t^2} + \frac{h_c}{2} l_{0t} \frac{\partial^2 w_{1c}}{\partial t^2} + \left(\frac{h_c}{2} \right)^2 l_{0t} \frac{\partial^2 w_{2c}}{\partial t^2} + \left(\frac{h_c}{2} \right)^3 l_{0t} \frac{\partial^2 w_{3c}}{\partial t^2} \right) \right) \\
\delta u_{2c} : &\left(1 - l^2 \frac{\partial^2}{\partial x^2}\right) \left(-\left(\frac{h_c}{2} \right)^2 \frac{\partial N_{xxb}}{\partial x} + \left(\frac{h_c}{2} \right)^2 \frac{\partial N_{xxt}}{\partial x} - 2M_{xzc} \right) \\
&= \left(1 - \mu^2 \frac{\partial^2}{\partial x^2}\right) \\
&\quad \times \left(\left(\frac{h_c}{2} \right)^2 \left(l_{0b} \frac{\partial^2 u_{0c}}{\partial t^2} + l_{1b} \frac{\partial^2 u_{1b}}{\partial t^2} + \frac{h_c}{2} l_{0b} \frac{\partial^2 u_{1b}}{\partial t^2} \right. \right. \\
&\quad \left. \left. - \frac{h_c}{2} l_{0b} \frac{\partial^2 u_{1c}}{\partial t^2} + \left(\frac{h_c}{2} \right)^2 l_{0b} \frac{\partial^2 u_{2c}}{\partial t^2} - \left(\frac{h_c}{2} \right)^3 l_{0b} \frac{\partial^2 u_{3c}}{\partial t^2} \right) \right. \\
&\quad \left. + \left(l_{2c} \frac{\partial^2 u_{0c}}{\partial t^2} + l_{3c} \frac{\partial^2 u_{1c}}{\partial t^2} + l_{4c} \frac{\partial^2 u_{2c}}{\partial t^2} + l_{5c} \frac{\partial^2 u_{3c}}{\partial t^2} \right) \right. \\
&\quad \left. + \left(\frac{h_c}{2} \right)^2 \left(l_{0t} \frac{\partial^2 u_{0c}}{\partial t^2} + l_{1t} \frac{\partial^2 u_{1t}}{\partial t^2} - \frac{h_c}{2} l_{0t} \frac{\partial^2 u_{1t}}{\partial t^2} + \frac{h_c}{2} l_{0t} \frac{\partial^2 u_{1c}}{\partial t^2} \right) \right. \\
&\quad \left. + \left(\frac{h_c}{2} \right)^2 l_{0t} \frac{\partial^2 u_{2c}}{\partial t^2} + \left(\frac{h_c}{2} \right)^3 l_{0t} \frac{\partial^2 u_{3c}}{\partial t^2} \right) \\
\delta w_{2c} : &\left(1 - l^2 \frac{\partial^2}{\partial x^2}\right) \left(-\left(\frac{h_c}{2} \right)^2 \frac{\partial N_{xzb}}{\partial x} + \left(\frac{h_c}{2} \right)^2 \frac{\partial N_{xzt}}{\partial x} + \frac{\partial P_{xzc}}{\partial x} \right)
\end{aligned}$$

$$\begin{aligned}
&= \left(1 - \mu^2 \frac{\partial^2}{\partial x^2}\right) \\
&\quad \times \left(\left(\frac{h_c}{2}\right)^2 \left(l_{0b} \frac{\partial^2 w_{0c}}{\partial t^2} - \frac{h_c}{2} l_{0b} \frac{\partial^2 w_{1c}}{\partial t^2} + \left(\frac{h_c}{2}\right)^2 l_{0b} \frac{\partial^2 w_{2c}}{\partial t^2} - \left(\frac{h_c}{2}\right)^3 l_{0b} \frac{\partial^2 w_{3c}}{\partial t^2} \right) \right. \\
&\quad \left. + \left(l_{2c} \frac{\partial^2 w_{0c}}{\partial t^2} + l_{3c} \frac{\partial^2 w_{1c}}{\partial t^2} + l_{4c} \frac{\partial^2 w_{2c}}{\partial t^2} + l_{5c} \frac{\partial^2 w_{3c}}{\partial t^2} \right) \right. \\
&\quad \left. + \left(\frac{h_c}{2}\right)^2 \left(l_{0t} \frac{\partial^2 w_{0c}}{\partial t^2} + \frac{h_c}{2} l_{0t} \frac{\partial^2 w_{1c}}{\partial t^2} + \left(\frac{h_c}{2}\right)^2 l_{0t} \frac{\partial^2 w_{2c}}{\partial t^2} + \left(\frac{h_c}{2}\right)^3 l_{0t} \frac{\partial^2 w_{3c}}{\partial t^2} \right) \right) \\
\delta u_{3c} : &\left(1 - \rho^2 \frac{\partial^2}{\partial x^2}\right) \left(-\left(\frac{h_c}{2}\right)^3 \frac{\partial N_{xxb}}{\partial x} + \left(\frac{h_c}{2}\right)^3 \frac{\partial N_{xxt}}{\partial x} - 3P_{xzc} \right) \\
&= \left(1 - \mu^2 \frac{\partial^2}{\partial x^2}\right) \\
&\quad \times \left(-\left(\frac{h_c}{2}\right)^3 \left(l_{0b} \frac{\partial^2 u_{0c}}{\partial t^2} + l_{1b} \frac{\partial^2 u_{1b}}{\partial t^2} + \frac{h_c}{2} l_{0b} \frac{\partial^2 u_{1b}}{\partial t^2} \right. \right. \\
&\quad \left. \left. - \frac{h_c}{2} l_{0b} \frac{\partial^2 u_{1c}}{\partial t^2} + \left(\frac{h_c}{2}\right)^2 l_{0b} \frac{\partial^2 u_{2c}}{\partial t^2} - \left(\frac{h_c}{2}\right)^3 l_{0b} \frac{\partial^2 u_{3c}}{\partial t^2} \right) \right. \\
&\quad \left. + \left(l_{3c} \frac{\partial^2 u_{0c}}{\partial t^2} + l_{4c} \frac{\partial^2 u_{1c}}{\partial t^2} + l_{5c} \frac{\partial^2 u_{2c}}{\partial t^2} + l_{6c} \frac{\partial^2 u_{3c}}{\partial t^2} \right) \right. \\
&\quad \left. + \left(\frac{h_c}{2}\right)^3 \left(l_{0t} \frac{\partial^2 u_{0c}}{\partial t^2} + l_{1t} \frac{\partial^2 u_{1t}}{\partial t^2} - \frac{h_c}{2} l_{0t} \frac{\partial^2 u_{1t}}{\partial t^2} + \frac{h_c}{2} l_{0t} \frac{\partial^2 u_{1c}}{\partial t^2} \right. \right. \\
&\quad \left. \left. + \left(\frac{h_c}{2}\right)^2 l_{0t} \frac{\partial^2 u_{2c}}{\partial t^2} + \left(\frac{h_c}{2}\right)^3 l_{0t} \frac{\partial^2 u_{3c}}{\partial t^2} \right) \right) \\
\delta w_{3c} : &\left(1 - \rho^2 \frac{\partial^2}{\partial x^2}\right) \left(-\left(\frac{h_c}{2}\right)^3 \frac{\partial N_{xzb}}{\partial x} + \left(\frac{h_c}{2}\right)^3 \frac{\partial N_{xzt}}{\partial x} + \frac{\partial Q_{xzc}}{\partial x} \right) \\
&= \left(1 - \mu^2 \frac{\partial^2}{\partial x^2}\right) \\
&\quad \times \left(-\left(\frac{h_c}{2}\right)^3 \left(l_{0b} \frac{\partial^2 w_{0c}}{\partial t^2} - \frac{h_c}{2} l_{0b} \frac{\partial^2 w_{1c}}{\partial t^2} + \left(\frac{h_c}{2}\right)^2 l_{0b} \frac{\partial^2 w_{2c}}{\partial t^2} - \left(\frac{h_c}{2}\right)^3 l_{0b} \frac{\partial^2 w_{3c}}{\partial t^2} \right) \right. \\
&\quad \left. + \left(l_{3c} \frac{\partial^2 w_{0c}}{\partial t^2} + l_{4c} \frac{\partial^2 w_{1c}}{\partial t^2} + l_{5c} \frac{\partial^2 w_{2c}}{\partial t^2} + l_{6c} \frac{\partial^2 w_{3c}}{\partial t^2} \right) \right. \\
&\quad \left. + \left(\frac{h_c}{2}\right)^3 \left(l_{0t} \frac{\partial^2 w_{0c}}{\partial t^2} + \frac{h_c}{2} l_{0t} \frac{\partial^2 w_{1c}}{\partial t^2} + \left(\frac{h_c}{2}\right)^2 l_{0t} \frac{\partial^2 w_{2c}}{\partial t^2} + \left(\frac{h_c}{2}\right)^3 l_{0t} \frac{\partial^2 w_{3c}}{\partial t^2} \right) \right) \\
\delta u_{1t} : &\left(1 - \rho^2 \frac{\partial^2}{\partial x^2}\right) \left(\frac{\partial M_{xxt}}{\partial x} - \frac{h_c}{2} \frac{\partial N_{xxt}}{\partial x} - N_{xzt} \right)
\end{aligned}$$

$$= \left(1 - \mu^2 \frac{\partial^2}{\partial x^2}\right) \left(\begin{aligned} &\left(l_{1t} \frac{\partial^2 u_{0c}}{\partial t^2} + l_{2t} \frac{\partial^2 u_{1t}}{\partial t^2} - \frac{h_c}{2} l_{1t} \frac{\partial^2 u_{1t}}{\partial t^2} + \frac{h_c}{2} l_{1t} \frac{\partial^2 u_{1c}}{\partial t^2} \right) \\ &+ \left(\frac{h_c}{2} \right)^2 l_{1t} \frac{\partial^2 u_{2c}}{\partial t^2} + \left(\frac{h_c}{2} \right)^3 l_{1t} \frac{\partial^2 u_{3c}}{\partial t^2} \\ &+ \frac{h_c}{2} \left(l_{0t} \frac{\partial^2 u_{0c}}{\partial t^2} + l_{1t} \frac{\partial^2 u_{1t}}{\partial t^2} - \frac{h_c}{2} l_{0t} \frac{\partial^2 u_{1t}}{\partial t^2} + \frac{h_c}{2} l_{0t} \frac{\partial^2 u_{1c}}{\partial t^2} \right) \\ &+ \left(\frac{h_c}{2} \right)^2 l_{0t} \frac{\partial^2 u_{2c}}{\partial t^2} + \left(\frac{h_c}{2} \right)^3 l_{0t} \frac{\partial^2 u_{3c}}{\partial t^2} \end{aligned} \right) \quad (20)$$

4. Semi-analytical solution procedure

The general differential quadrature method (GDQM) is approximating the derivative of an unknown function using the weighted values of the function in certain points on its domain [90,91]. Therefore, the derivative of the function could be expressed as follows:

$$\frac{\partial^n f}{\partial x^n} = \sum_{m=1}^M g^{(n)}_{j,m} f_{m,k} \quad (21)$$

The weighting function $g^{(n)}$ is defined as recursive relations. First, $g^{(1)}$ is defined as follows:

$$\begin{aligned} g_{ij}^{(1)} &= - \sum_{j=1, i \neq j}^n g_{ij}^{(1)} \quad i = j \\ g_{ij}^{(1)} &= \frac{1}{(x_i - x_j)} \frac{M(x_i)}{M(x_j)} \quad i, j = 1, 2, \dots, n \text{ and } i \neq j \end{aligned} \quad (22)$$

where $M(x_i)$ is defined as follows:

$$M(x_i) = \prod_{j=1, j \neq i}^n (x_i - x_j) \quad (23)$$

Once $g^{(1)}$ is determined the following $g^{(n)}$ could be determined using the below recursive relations:

$$\begin{aligned} g_{ii}^{(n)} &= - \sum_{j=1, i \neq j}^n g_{ij}^{(n)} \quad 1 \leq n \leq N-1 \text{ while } j, i = 1, 2, \dots, N \\ g_{ij}^{(n)} &= r \left[g_{ij}^{(n-1)} g_{ij}^{(1)} - \frac{g_{ij}^{(n-1)}}{(x_i - x_j)} \right] \quad i \neq j, 2 \leq n \leq N-1 \text{ while } j, i = 1, 2, \dots, N. \end{aligned} \quad (24)$$

The aforementioned certain points, in which the weighted function values are utilized, are determined using Chebyshev polynomial grid points:

$$x_i = \frac{L}{2} \left(1 - \cos \left(\frac{(i-1)}{(N_i-1)} \pi \right) \right) \quad i = 1, 2, 3, \dots, N_i \quad (25)$$

Finally, the differential equations are converted to a set of algebraic equations whose unknowns are the function values at Chebyshev seeds [93,94]:

$$\left\{ \begin{bmatrix} [\mathcal{M}_{dd}] & [\mathcal{M}_{db}] \\ [\mathcal{M}_{bd}] & [\mathcal{M}_{bb}] \end{bmatrix} \varpi^2 + \begin{bmatrix} [\mathcal{K}_{dd}] & [\mathcal{K}_{db}] \\ [\mathcal{K}_{bd}] & [\mathcal{K}_{bb}] \end{bmatrix} \right\} \begin{Bmatrix} \Xi_d \\ \Xi_b \end{Bmatrix} = 0 \quad (26)$$

Natural frequencies of the structure are obtained by solving Eq. (26):

$$\bar{\omega} = \frac{\sqrt{\text{Real}(\varpi^2)} L^2}{h} \sqrt{\frac{\rho_c}{E_c}} \quad (27a)$$

$$\text{Modal Loss Factor} = \frac{\text{Image}(\varpi^2)}{\text{Real}(\varpi^2)} \quad (27b)$$

5. Deep learning-based comparative study

An artificial intelligence-based method is introduced in this section to predict the natural frequency of the structure. In this regard, a deep neural network (DNN) is utilized with the inputs as influencing factors comprising from $X = \left\{ \theta, E, n_x, n_z, \frac{R_i}{h}, \frac{L}{R_i}, \frac{h_f}{h} \right\}^T$ and the output to be $\hat{Y} = \bar{\omega}$. The hat upon the output notation \hat{Y} indicates that the value is calculated by DNN. The output of the DNN is compared to the actual value provided by numerical methods. The comparison means calculating their differences to find out about the accuracy of the network. In the training process, the data obtained from numerical simulation are fed into the DNN, and in each iteration the loss function (error) is calculated. Several types of loss functions could be utilized in this network. However, for the aim of this study means squared error (MSE) as defined by

$$\text{MSE} = \frac{1}{n} \sum_{i=1}^n (Y - \hat{Y})^2 \quad (28)$$

is utilized. The aim of the training process is to reduce the error value to a minimum value [92]. The minimum value is reached when the training and validating loss function starts to depart. In the validation process the DNN checks itself to avoid over-fitting the data. Optimization of the loss function is called back-propagation and several approaches have been proposed to reduce the error in each step in an effective way. In the present study, we employed the ADADELTA optimization procedure in which the learning rate is set automatically and there is no need for intervening by the user, unlike the decent gradient method. Also, this method's sensitivity to hyperparameters is extremely low. Therefore, it is a perfect option for this study.

6. Result

In the following, the effects of several parameters on the frequency responses of the cylindrical sandwich structure are presented and discussed. First, the material properties of each layer of the composite are presented in Table 1.

Table 1. Mechanical properties of the sandwich composite layers.

Ceramic (Al ₂ O ₃)	Metal (SUS304)	Electro rheological fluid [95]
$E_c = 348.43 \times 10^9 [\text{Pa}]$	$E_m = 201.04 \times 10^9 [\text{Pa}]$	$G' \left(\frac{\text{KV}}{\text{mm}} \right) = 50000 \times E^2$
$\nu_c = 0.2400$	$\nu_m = 0.3262$	$G'' \left(\frac{\text{KV}}{\text{mm}} \right) = 2600 \times E + 1700$
$\rho_c = 2370 \left[\frac{\text{Kg}}{\text{m}^3} \right]$	$\rho_m = 8166 \left[\frac{\text{Kg}}{\text{m}^3} \right]$	$\rho_{\text{ER}} \left(\frac{\text{kg}}{\text{m}^3} \right) = 1200$

Table 2. Natural frequencies and modal loss factors of the sliding simply supported beam with $h_b = 5$ [mm], $h_t = 2.5$ [mm], $h_c = 0.5$ [mm], $L = 300$ [mm], $\rho_b = \rho_t = 7800$ [kg/m³], $\rho_c = 2000$ [kg/m³], $E_b = E_t = 207$ Gpa, $\nu = 0.3$, $G_b = G_t = 79.6154$ [Gpa], $G_c = 0.2615(1 + 0.38i)$ [MPa].

		Mode 1	Mode 2	Mode 3	Mode 4
Natural frequency (Hz)	Present work	739.908	2942.74	6607.63	11715.12
	Ref. [96]	740.306	2944.89	6608.93	11717.3
	Ref. [97]	740.489	2947.775	6623.477	11763.052
	Ref. [98]	740.564	2949.00	6629.68	11782.61
Modal loss factor (%)	Present work	0.43781	0.11381	0.050126	0.026521
	Ref. [96]	0.448204	0.114795	0.0512581	0.0288852
	Ref. [97]	0.44818	0.11477	0.051232	0.028859
	Ref. [98]	0.44825	0.11484	0.051306	0.028932

6.1. Validation

The novel ER material and semi-analytical approach described in the previous sections need to be verified by comparing the results of this approach in solving exactly identical problems given in published articles. Therefore, three references are chosen for comparing the results, as presented in Table 2. The obtained values for natural frequencies in different modes from the present approach show acceptable agreement with the result of other references on similar subjects. Therefore, the current method is reliable and could be utilized for further analyses.

6.2. Convergency study

The GDQM method necessitates using several grids in different directions based on the dimensions of the problem. The number of seeds in each direction determines the accuracy of the results. Thus, a convergence study is conducted to discover a minimum number of seeds in each direction. In Tables 3 and 4, convergency of natural frequency is presented for different boundary conditions including clamped–clamped (C–C), clamped-simple (C–S), and simple-simple (S–S) boundary conditions. The values of the natural frequency indicate that at least 9 seeds in each direction are required to have convergent results based on the values of dimensionless boundary conditions.

In addition to the natural frequency, the convergence behavior of the loss factor η indicates that the minimum number of seeds in GDQM should be kept equal to 9 in all numerical evaluations.

The DNN method used also has several parameters which are controlled by the user. The maximum value of MSE could be at the desire of the user. In Table 5, the values of the natural frequency are presented as a function of parameter E and MSE . As can be observed,

Table 3. Natural frequency ($\bar{\omega}_{11}$) convergence study as a function of the number of seeds in the GDQM of system with $\frac{l}{h} = 50$, $\mu = h$, $l = h$, $E = 5 \left[\frac{\text{KV}}{\text{mm}} \right]$, $h_b = h_t = h_c = \frac{h}{3}$, and $n_x = n_z = 0.5$.

Boundary condition's	N				
	5	7	9	11	13
SS	0.0695	0.0687	0.0685	0.0685	0.0685
CS	0.1247	0.1238	0.1235	0.1235	0.1235
CC	0.1939	0.1930	0.1928	0.1928	0.1928

Table 4. Loss factor convergence study as a function of the number of seeds in GDQM of the system with $\frac{l}{h} = 50$, $\mu = h$, $l = h$, $E = 5 \left[\frac{\text{KV}}{\text{mm}} \right]$, $h_b = h_t = h_c = \frac{h}{3}$, and $n_x = n_z = 0.5$.

Boundary conditions	N				
	5	7	9	11	13
SS	0.0582	0.0576	0.0575	0.0575	0.0575
CS	0.2028	0.02018	0.2015	0.2015	0.2015
CC	0.3591	0.3582	0.3580	0.3580	0.3580

Table 5. Prediction on the real part of frequency performance using the DNN model for train data for various E and MSE parameters.

	Fit	Predicted			
		$MSE_{\text{Train}} = 0.62 \times 10^{-5}$	$MSE_{\text{Train}} = 0.9 \times 10^{-5}$	$MSE_{\text{Train}} = 0.95 \times 10^{-5}$	$MSE_{\text{Train}} = 10^{-6}$
$E = 1 \left[\frac{\text{KV}}{\text{mm}} \right]$	0.0780	0.0854	0.0785	0.0783	0.0783
$E = 2 \left[\frac{\text{KV}}{\text{mm}} \right]$	0.1558	0.1894	0.1562	0.1560	0.1560
$E = 3 \left[\frac{\text{KV}}{\text{mm}} \right]$	0.2337	0.2682	0.2342	0.2340	0.2340

increasing the value of E results an increase in the natural frequency while a decrease in MSE only improves the accuracy of the DNN network results.

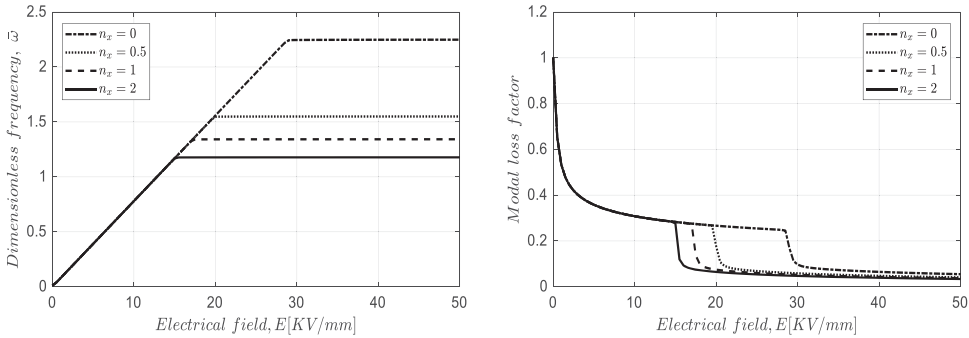
In addition to the natural frequency effect of the parameter E on the loss factor is also investigated in Table 6. Increasing the value of the parameter E leads to a decrease in the loss factor which is favorable in such structures. On the other hand, similar to the natural frequency, a decrease in MSE only improves the accuracy of the DNN prediction in loss factor evaluation.

6.3. Parametric study

In the following, we attempt to shed light on the effects of different parameters on the vibrational behavior of the cylindrical composite structure with ER fluid core. The effect of different values of the grading index of the FG layers is considered. In doing so, Figure 2 shows the effect of the FG index in the x direction on dimensionless natural frequency and loss factor of the ER fluid core for the range of applied external electrical fields. It is observed that increasing electrical load results in an increase in the natural frequency of the structure. However, this increase stops at a critical value of the electrical load values depending on the

Table 6. Prediction of the loss factor performance using the DNN model for train data for various E and MSE parameters.

	Fit	Predicted			
		$MSE_{Train} = 0.62 \times 10^{-5}$	$MSE_{Train} = 0.9 \times 10^{-5}$	$MSE_{Train} = 0.95 \times 10^{-5}$	$MSE_{Train} = 10^{-6}$
$E = 1 \begin{bmatrix} \text{KV} \\ \text{mm} \end{bmatrix}$	0.5328	0.5792	0.5333	0.5330	0.5330
$E = 2 \begin{bmatrix} \text{KV} \\ \text{mm} \end{bmatrix}$	0.4439	0.4791	0.4745	0.4742	0.4742
$E = 3 \begin{bmatrix} \text{KV} \\ \text{mm} \end{bmatrix}$	0.4024	0.4374	0.4030	0.4027	0.4027

**Figure 2.** Effect of the FG index in the x-direction n_x on the natural frequency and loss factor of the structure in a range of applied external electrical loads. $\frac{l}{h} = 50, \mu = h, l = h, h_b = h_t = h_c = \frac{h}{3}$ and $n_z = 0$.

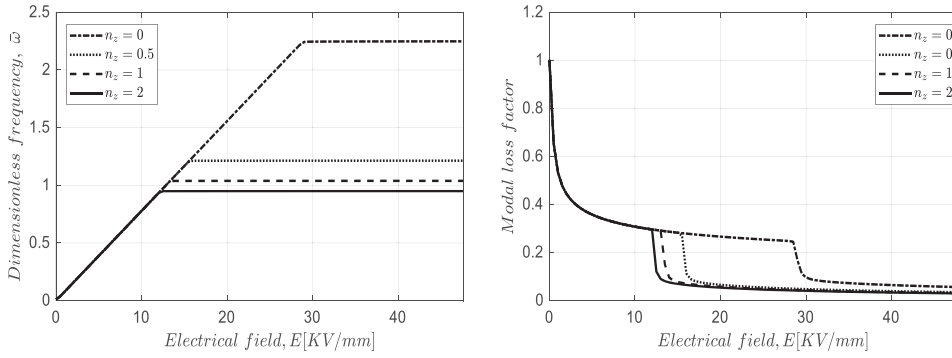
FG index. Afterward, the natural frequency of the structure becomes constant for every n_x . Increasing the FG index n_x , on the other hand, reduces the stable value of the natural frequency. Up to a certain value of the electrical field load, the indexing coefficient has no effect on the natural frequency of the structure as all the curves corresponding to the different indices values coincide. The effect of the FG index n_x on the loss factor is strongly dependent on the electrical load. In the low and high values of the applied electrical fields, the FG index has no effect on the loss factor as all the curves for various values of index n_x coincide. However, in the midrange values of the applied electrical loads, there is a downward step in the loss factor curves in the critical value of the electrical load. After this step, neither the electrical field nor the index n_x has light effects on the loss factor. The increasing index n_x results in sharp reduction of the loss factor in lower values of the electrical field.

The trained DNN is capable of presenting closed-form relations for natural frequencies of the structure. The closed-form polynomial relation of the natural frequency as a function of parameter E for different values of FG indices is presented in Table 7.

Similar to the effect of n_x , the index of the FG layer in the z-direction, n_z , is depicted in Figure 3. The effect of n_z is very similar to the effects of the index n_x . The only difference is that in lower values of the applied electrical load, abrupt changes in the behavior of the natural frequency and loss factor are seen. Moreover, it is seen that an increase in the FG index in both directions causes a decrease in the applied critical electrical load.

Table 7. The closed-form relation of the dimensionless natural frequency of the sandwich structure as predicted using DNN ($z = E$, $y = \bar{\omega}$).

	$\bar{\omega}$
$n_x = 0$	$y = 0.0011 \times z^{10} + 0.037 \times z^9 + 0.0057 \times z^8 - 0.27 \times z^7 - 0.086 \times z^6 + 0.73 \times z^5 + 0.31 \times z^4 - 0.85 \times z^3 - 0.67 \times z^2 + 1.1 \times z + 2$
$n_x = 0.5$	$y = 0.019 \times z^{10} - 0.037 \times z^9 - 0.14 \times z^8 + 0.28 \times z^7 + 0.34 \times z^6 - 0.75 \times z^5 - 0.25 \times z^4 + 0.92 \times z^3 - 0.37 \times z^2 - 0.03 \times z + 1.6$
$n_x = 1$	$y = 0.035 \times z^{10} - 0.009 \times z^9 - 0.28 \times z^8 + 0.089 \times z^7 + 0.8 \times z^6 - 0.34 \times z^5 - 0.96 \times z^4 + 0.62 \times z^3 + 0.13 \times z^2 - 0.095 \times z + 1.3$
$n_x = 2$	$y = 0.018 \times z^{10} + 0.019 \times z^9 - 0.16 \times z^8 - 0.11 \times z^7 + 0.55 \times z^6 + 0.15 \times z^5 - 0.81 \times z^4 + 0.16 \times z^3 + 0.24 \times z^2 - 0.05 \times z + 1.2$

**Figure 3.** Effect of the FG index in the z -direction n_z on the natural frequency and loss factor of the structure in a range of applied external electrical loads. $\frac{l}{h} = 50$, $\mu = h$, $l = h$, $h_b = h_t = h_c = \frac{h}{3}$ and $n_x = 0$.**Table 8.** The closed-form expressions of the natural frequency of the sandwich nano pipe by the DNN method ($z = E$, $y = \bar{\omega}$).

	$\bar{\omega}$
$n_z = 0$	$y = 0.0011 \times z^{10} + 0.037 \times z^9 + 0.0057 \times z^8 - 0.27 \times z^7 - 0.086 \times z^6 + 0.73 \times z^5 + 0.31 \times z^4 - 0.85 \times z^3 - 0.67 \times z^2 + 1.1 \times z + 2$
$n_z = 0.5$	$y = 0.024 \times z^{10} + 0.013 \times z^9 - 0.2 \times z^8 - 0.07 \times z^7 + 0.65 \times z^6 + 0.048 \times z^5 - 0.9 \times z^4 + 0.27 \times z^3 + 0.24 \times z^2 - 0.064 \times z + 1.2$
$n_z = 1$	$y = -0.0067 \times z^{10} + 0.031 \times z^9 + 0.024 \times z^8 - 0.21 \times z^7 + 0.059 \times z^6 + 0.43 \times z^5 - 0.32 \times z^4 - 0.16 \times z^3 + 0.14 \times z^2 + 0.0045 \times z + 1$
$n_z = 2$	$y = -0.02 \times z^{10} + 0.03 \times z^9 + 0.13 \times z^8 - 0.21 \times z^7 - 0.24 \times z^6 + 0.49 \times z^5 + 0.026 \times z^4 - 0.27 \times z^3 + 0.043 \times z^2 + 0.03 \times z + 0.95$

Closed-form polynomial equations of the natural frequency as a function of the parameter E are presented in Table 8 as predicted by DNN.

Figure 4 presents the effect of the parameter μ on the natural frequency and loss factor of the structure. Effects of the applied external electrical field are similar in all conditions as discussed above. However, as the parameter μ increases the results in a decrease in the natural frequency and loss factor. Moreover, a change in the parameter μ does not change the critical electrical load.

The effect of the parameter E on the natural frequency of the cylindrical structure is predicted by DNN for different values of the parameter μ as presented in Table 9 in the form

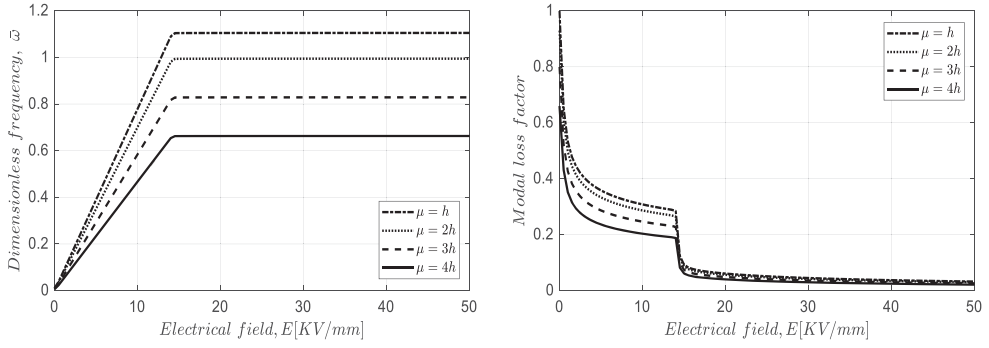


Figure 4. Effect of the nonlocal parameter μ on the natural frequency and loss factor of the structure in a range of applied external electrical loads. $\frac{l}{h} = 50$, $l = h$, $h_b = h_t = h_c = \frac{h}{3}$, and $n_x = n_z = 0.5$.

Table 9. The closed-form relation of the dimensionless natural frequency of the sandwich structure as predicted using DNN ($z = E$, $y = \bar{\omega}$).

	$\bar{\omega}$
$\mu = h$	$y = 0.0054 \times z^{10} + 0.027 \times z^9 - 0.069 \times z^8 - 0.17 \times z^7 + 0.31 \times z^6 + 0.32 \times z^5 - 0.58 \times z^4 - 0.02 \times z^3 + 0.2 \times z^2 - 0.021 \times z + 1.1$
$\mu = 2h$	$y = 0.0048 \times z^{10} + 0.024 \times z^9 - 0.062 \times z^8 - 0.16 \times z^7 + 0.28 \times z^6 + 0.29 \times z^5 - 0.52 \times z^4 - 0.018 \times z^3 + 0.18 \times z^2 - 0.019 \times z + 0.99$
$\mu = 3h$	$y = 0.004 \times z^{10} + 0.02 \times z^9 - 0.051 \times z^8 - 0.13 \times z^7 + 0.23 \times z^6 + 0.24 \times z^5 - 0.43 \times z^4 - 0.015 \times z^3 + 0.15 \times z^2 - 0.016 \times z + 0.82$
$\mu = 4h$	$y = 0.0032 \times z^{10} + 0.016 \times z^9 - 0.041 \times z^8 - 0.1 \times z^7 + 0.18 \times z^6 + 0.19 \times z^5 - 0.35 \times z^4 - 0.012 \times z^3 + 0.12 \times z^2 - 0.013 \times z + 0.66$

Table 10. The closed-form relation of the dimensionless natural frequency of the sandwich structure as predicted using DNN ($z = E$, $y = \bar{\omega}$).

	$\bar{\omega}$
$l = h$	$y = 0.0054 \times z^{10} + 0.027 \times z^9 - 0.069 \times z^8 - 0.17 \times z^7 + 0.31 \times z^6 + 0.32 \times z^5 - 0.58 \times z^4 - 0.02 \times z^3 + 0.2 \times z^2 - 0.021 \times z + 1.1$
$l = 2h$	$y = 0.0062 \times z^{10} + 0.031 \times z^9 - 0.079 \times z^8 - 0.2 \times z^7 + 0.35 \times z^6 + 0.37 \times z^5 - 0.67 \times z^4 - 0.023 \times z^3 + 0.23 \times z^2 - 0.024 \times z + 1.3$
$l = 3h$	$y = 0.0077 \times z^{10} + 0.039 \times z^9 - 0.099 \times z^8 - 0.25 \times z^7 + 0.44 \times z^6 + 0.47 \times z^5 - 0.84 \times z^4 - 0.029 \times z^3 + 0.29 \times z^2 - 0.03 \times z + 1.6$
$l = 4h$	$y = 0.01 \times z^{10} + 0.052 \times z^9 - 0.13 \times z^8 - 0.33 \times z^7 + 0.58 \times z^6 + 0.61 \times z^5 - 1.1 \times z^4 - 0.038 \times z^3 + 0.39 \times z^2 - 0.04 \times z + 2.1$

of polynomial functions. The ability of the DNN network to provide a polynomial approximation of the functions is very useful in this type of problem in which numerical solving equation is highly time-consuming.

The effect of the gradient parameter l on the natural frequency, loss factor, and critical electrical field is shown in Figure 5. This figure indicates that in contrast to the effect of the nonlocal parameter, increasing the length scale parameter improves the structure's natural frequency and loss factor. Similar to the nonlocal parameter, a change in the length scale parameter does not affect the critical value of the electrical load.

Table 10 presents the outcome of DNN as a polynomial equation that expresses natural frequency dependency on the parameter E as polynomials of the 10th degree for different values of gradient length scale parameter.

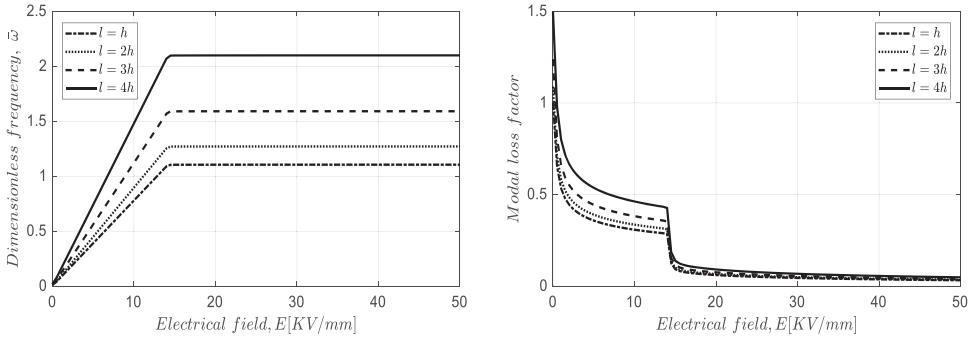


Figure 5. Effect of gradient length scale parameter l on the natural frequency and loss factor of the structure in a range of applied external electrical loads. $\frac{l}{h} = 50$, $\mu = h$, $h_b = h_t = h_c = \frac{h}{3}$, and $n_x = n_z = 0.5$.

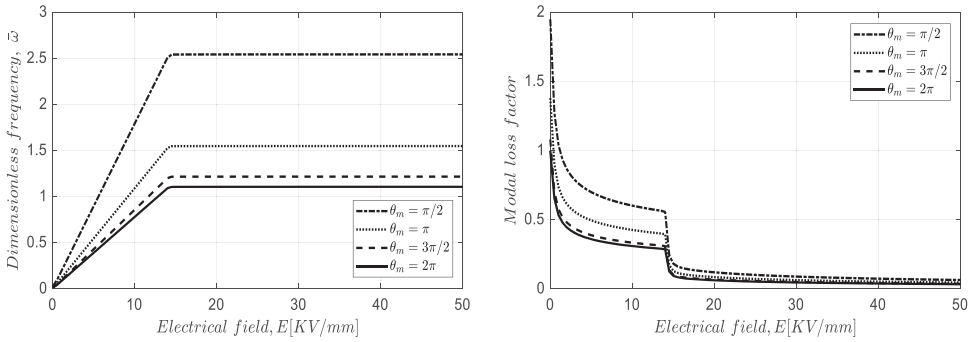


Figure 6. Effect of parameter θ_m on the natural frequency and loss factor of the structure in a range of applied external electrical loads. $\frac{l}{h} = 50$, $\mu = h$, $l = h$, $h_b = h_t = h_c = \frac{h}{3}$, and $n_x = n_z = 0.5$.

A different slice of the cylinder in the axial direction is considered to observe the effect of the section angle θ_m on the natural frequency and loss factor in different applied electrical loads. It is seen that increasing the value of the parameter θ_m results in both a decrease in natural frequencies and a loss factor in all values of the applied electrical load. Moreover, alternation in the parameter θ_m has not changed the value of the critically applied electrical field Figure 6.

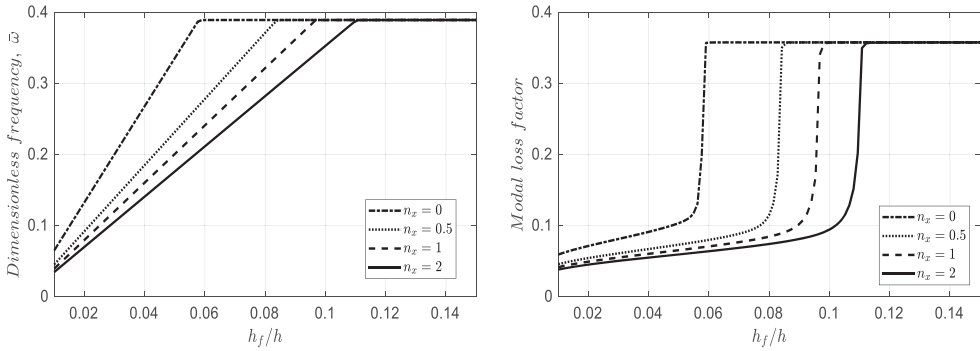
The results of the DNN analysis in the form of polynomials relating natural frequency to the parameter E are provided in Table 11 for different values of the parameter θ_m .

The effect of the thickness of ER fluid core layer on the natural frequency and loss factor is observed in Figure 7 for different FG index n_x values. It is seen that the critical saturated natural frequency is not dependent on the index n_x . The final value of the loss factor in the high value of thickness ratio also does not dependent on the index n_x . However, in lower ER core thicknesses increasing in index number results in a decrease in both natural frequency and loss factor.

The results of the DNN analysis in the form of polynomials relating natural frequency to the thickness ratio $\frac{h_f}{h}$ are provided in Table 12 for different values of the parameter n_x .

Table 11. The closed-form relation of the dimensionless natural frequency of the sandwich structure as predicted using DNN ($z = E$, $y = \bar{\omega}$).

	$\bar{\omega}$
$\theta_m = \frac{\pi}{2}$	$y = 0.012 \times z^{10} + 0.062 \times z^9 - 0.16 \times z^8 - 0.4 \times z^7 + 0.71 \times z^6 + 0.74 \times z^5 - 1.3 \times z^4 - 0.046 \times z^3 + 0.47 \times z^2 - 0.048 \times z + 2.5$
$\theta_m = \pi$	$y = 0.0075 \times z^{10} + 0.038 \times z^9 - 0.096 \times z^8 - 0.24 \times z^7 + 0.43 \times z^6 + 0.45 \times z^5 - 0.81 \times z^4 - 0.028 \times z^3 + 0.28 \times z^2 - 0.029 \times z + 1.5$
$\theta_m = \frac{3\pi}{2}$	$y = 0.0059 \times z^{10} + 0.03 \times z^9 - 0.075 \times z^8 - 0.19 \times z^7 + 0.34 \times z^6 + 0.36 \times z^5 - 0.64 \times z^4 - 0.022 \times z^3 + 0.22 \times z^2 - 0.023 \times z + 1.2$
$\theta_m = 2\pi$	$y = 0.0054 \times z^{10} + 0.027 \times z^9 - 0.069 \times z^8 - 0.17 \times z^7 + 0.31 \times z^6 + 0.32 \times z^5 - 0.58 \times z^4 - 0.02 \times z^3 + 0.2 \times z^2 - 0.021 \times z + 1.1$

**Figure 7.** Effect of the FG index n_x on the natural frequency and loss factor of the structure in a range of different thicknesses of ER fluid core layer. $\frac{L}{h} = 50$, $\mu = h$, $l = h$, $E = 5 \left[\frac{\text{KV}}{\text{mm}} \right]$, and $n_x = 0$.**Table 12.** The closed-form relation of the dimensionless natural frequency of the sandwich cylindrical sandwich structure as predicted using DNN ($z = \frac{h_f}{h}$, $y = \bar{\omega}$).

	$\bar{\omega}$
$n_x = 0$	$y = 0.0083 \times z^{10} - 0.0016 \times z^9 - 0.067 \times z^8 + 0.018 \times z^7 + 0.19 \times z^6 - 0.075 \times z^5 - 0.23 \times z^4 + 0.14 \times z^3 + 0.034 \times z^2 - 0.023 \times z + 0.39$
$n_x = 0.5$	$y = -0.0052 \times z^{10} + 0.0032 \times z^9 + 0.043 \times z^8 - 0.023 \times z^7 - 0.13 \times z^6 + 0.059 \times z^5 + 0.2 \times z^4 - 0.066 \times z^3 - 0.19 \times z^2 + 0.13 \times z + 0.37$
$n_x = 1$	$y = 0.0041 \times z^{10} + 0.0043 \times z^9 - 0.031 \times z^8 - 0.034 \times z^7 + 0.082 \times z^6 + 0.096 \times z^5 - 0.082 \times z^4 - 0.13 \times z^3 - 0.025 \times z^2 + 0.18 \times z + 0.32$
$n_x = 2$	$y = 0.00056 \times z^{10} - 0.0035 \times z^9 - 0.008 \times z^8 + 0.023 \times z^7 + 0.037 \times z^6 - 0.042 \times z^5 - 0.072 \times z^4 + 0.003 \times z^3 + 0.025 \times z^2 + 0.15 \times z + 0.28$

The effect of the thickness of ER fluid core layer on the natural frequency and loss factor is observed in Figure 8 for different FG index n_z values. It is seen that the critical saturated natural frequency is not dependent on the index n_z . The final value of the loss factor in the high value of thickness ratio also does not dependent on the index n_z . However, in lower ER core thicknesses increasing in index number results in a decrease in both natural frequency and loss factor.

The results of the DNN analysis in the form of polynomials relating natural frequency to the thickness ratio $\frac{h_f}{h}$ are provided in Table 13 for different values of the parameter n_z .

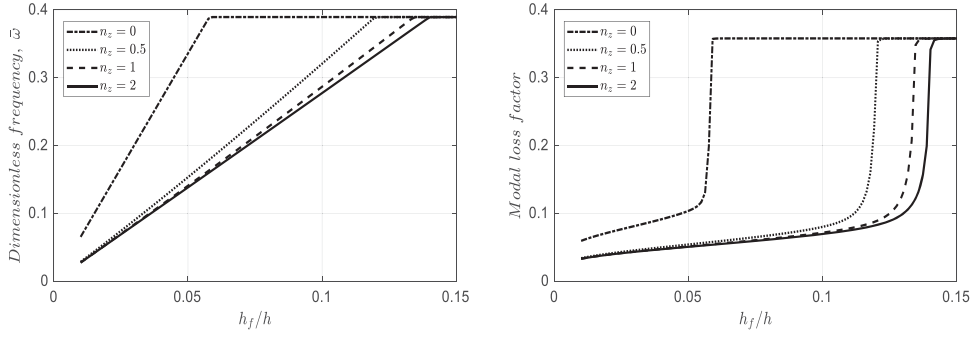


Figure 8. Effect of the FG index n_z on the natural frequency and loss factor of the structure in a range of different thicknesses of ER fluid core layer. $\frac{l}{h} = 50$, $\mu = h$, $l = h$, $E = 5 \left[\frac{KV}{mm} \right]$, and $n_z = 0$.

Table 13. The closed-form relation of the dimensionless natural frequency of the sandwich structure as predicted using DNN $\left(z = \frac{h_f}{h}, y = \bar{\omega} \right)$.

	$\bar{\omega}$
$n_z = 0$	$y = 0.0083 \times z^{10} - 0.0016 \times z^9 - 0.067 \times z^8 + 0.018 \times z^7 + 0.19 \times z^6 - 0.075 \times z^5 - 0.23 \times z^4 + 0.14 \times z^3 + 0.034 \times z^2 - 0.023 \times z + 0.39$
$n_z = 0.5$	$y = -0.0035 \times z^{10} - 0.0025 \times z^9 + 0.026 \times z^8 + 0.02 \times z^7 - 0.06 \times z^6 - 0.052 \times z^5 + 0.043 \times z^4 + 0.036 \times z^3 - 0.0048 \times z^2 + 0.13 \times z + 0.25$
$n_z = 1$	$y = 0.0019 \times z^{10} + 0.0022 \times z^9 - 0.012 \times z^8 - 0.014 \times z^7 + 0.022 \times z^6 + 0.024 \times z^5 - 0.015 \times z^4 - 0.014 \times z^3 + 0.005 \times z^2 + 0.12 \times z + 0.23$
$n_z = 2$	$y = 0.00084 \times z^{10} + 0.00014 \times z^9 - 0.0066 \times z^8 - 0.0024 \times z^7 + 0.016 \times z^6 + 0.0064 \times z^5 - 0.015 \times z^4 - 0.0051 \times z^3 + 0.0046 \times z^2 + 0.12 \times z + 0.22$

Table 14. The closed-form relation of the dimensionless natural frequency of the sandwich cylindrical sandwich structure as predicted using DNN $\left(z = \frac{h_f}{h}, y = \bar{\omega} \right)$.

	$\bar{\omega}$
$E = 1 \left[\frac{KV}{mm} \right]$	$y = 0.0017 \times z^{10} - 0.0023 \times z^9 - 0.01 \times z^8 + 0.014 \times z^7 + 0.017 \times z^6 - 0.024 \times z^5 - 0.0098 \times z^4 + 0.014 \times z^3 + 0.0016 \times z^2 - 0.0019 \times z + 0.078$
$E = 2 \left[\frac{KV}{mm} \right]$	$y = 0.002 \times z^{10} + 0.0021 \times z^9 - 0.018 \times z^8 - 0.012 \times z^7 + 0.062 \times z^6 + 0.015 \times z^5 - 0.091 \times z^4 + 0.02 \times z^3 + 0.026 \times z^2 - 0.0058 \times z + 0.15$
$E = 3 \left[\frac{KV}{mm} \right]$	$y = -0.0039 \times z^{10} - 0.0014 \times z^9 + 0.032 \times z^8 + 0.01 \times z^7 - 0.099 \times z^6 - 0.026 \times z^5 + 0.15 \times z^4 + 0.028 \times z^3 - 0.13 \times z^2 + 0.049 \times z + 0.23$
$E = 4 \left[\frac{KV}{mm} \right]$	$y = 0.0039z^{10} + 0.00081z^9 - 0.032z^8 - 0.0089z^7 + 0.092z^6 + 0.036z^5 - 0.11z^4 - 0.069z^3 + 0.018z^2 + 0.14z + 0.24$

In Figure 9, the effect of the parameter E on the natural frequency and loss factor curves are depicted for a range of ER core thickness ratios. Increasing parameter E causes an increase in natural frequency and a decrease in loss factor. However, an increase in the natural frequency does not occur until reaching the saturated natural frequency, while in the case of the loss factor in all ranges of thickness ratio, the loss factor reduces as a result of the increasing parameter E .

The results of the DNN analysis in the form of polynomials relating natural frequency to the thickness ratio $\frac{h_f}{h}$ are provided in the table for different values of the parameter E .

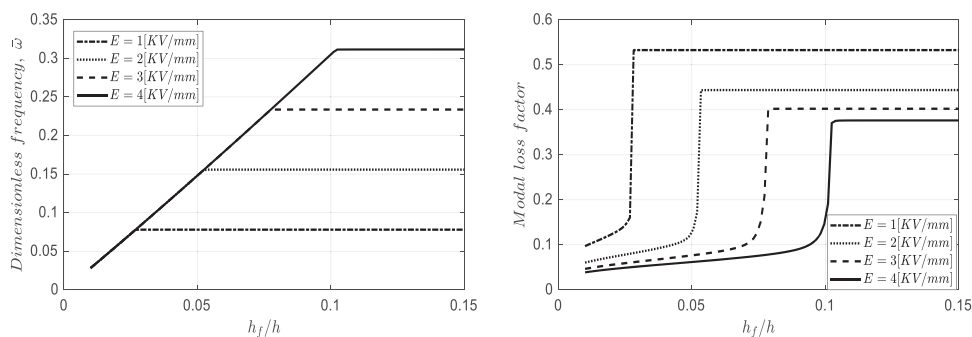


Figure 9. Effect of FG parameter E on the natural frequency and loss factor of the structure in a range of different thicknesses of ER fluid core layer. $\frac{l}{h} = 50$, $\mu = h$, $l = h$, and $n_x = n_z = 0.5$.

7. Conclusion

In the present study, for the first time, the effects of using an electrical field in improving the dynamic stability of nanostructure containing ER fluids were presented. In this regard, a cylindrical sandwich structure with the inner and outer layers composed of two-directional functionally graded (2D-FG) material and ER fluid core was considered. Employing energy methods and modified power law the equations of motion of the structure were derived. Between FG and ER layers, compatibility conditions are imposed in terms of displacement and strains. Moreover, to bypass computational complications, the inputs and outputs were utilized for training a deep neural network (DNN). In this way, the inputs and outputs were related to each other through the regression method without numerically solving the equations of motion all over again. Finally, the effects of different parameters on the vibrational characteristics of the structure were presented. The main results of this survey could be encapsulated below:

- The effect of the FG indices n_x and n_z on the loss factor is strongly dependent on the electrical load.
- In the low and high values of the applied electrical fields, the FG index has no effect on the loss factor.
- Changes in the nonlocal and gradient length scale parameters do not change the critical electrical load.
- Increasing electrical load results in an increase in the natural frequency of the structure. However, this increase stops at a critical value of the electrical load values.

Disclosure statement

No potential conflict of interest was reported by the author(s).

References

- [1] Huang Xiaoping, Hao Huadong, Oslub Khaled, et al. Dynamic stability/instability simulation of the rotary size-dependent functionally graded microsystem. *Engineering with Computers*. 2022;38(S5):4163–4179. <http://dx.doi.org/10.1007/s00366-021-01399-3>.

- [2] Al-Furjan M. S. H, Bolandi Seyedeh Yasaman, Habibi Mostafa, et al. Enhancing vibration performance of a spinning smart nanocomposite reinforced microstructure conveying fluid flow. *Engineering with Computers*. 2022;38(S5):4097–4112. <http://dx.doi.org/10.1007/s00366-020-01255-w>.
- [3] Cheshmeh E, Karbon M, Eyvazian A, et al. Buckling and vibration analysis of FG-CNTRC plate subjected to thermo-mechanical load based on higher order shear deformation theory. *Mech Based Des Struct Mach*. 2020;50:1–24.
- [4] Moayedi H, Habibi M, Safarpour H, et al. Buckling and frequency responses of a graphene nanoplatelet reinforced composite microdisk. *Int J Appl Mech*. 2019;11:Article 1950102.
- [5] Al-Furjan M, Habibi M, Chen G, et al. Chaotic simulation of the multi-phase reinforced thermo-elastic disk using GDQM. *Eng Comput*. 2020;38:1–24.
- [6] Jalali MR, Shavalipour A, Safarpour M, et al. Frequency analysis of a graphene platelet–reinforced imperfect cylindrical panel covered with piezoelectric sensor and actuator. *The Journal of Strain Analysis for Engineering Design*. 2020;55:181–196.
- [7] Habibi M, Safarpour M, Safarpour H. Vibrational characteristics of a FG-GPLRC viscoelastic thick annular plate using fourth-order Runge-Kutta and GDQ methods. *Mech Based Des Struct Mach*. 2020;50:1–22.
- [8] Al-Furjan M, Safarpour H, Habibi M, et al. A comprehensive computational approach for nonlinear thermal instability of the electrically FG-GPLRC disk based on GDQ method. *Eng Comput*. 2020;38:1–18.
- [9] He X, Ding J, Habibi M, et al. Non-polynomial framework for bending responses of the multi-scale hybrid laminated nanocomposite reinforced circular/annular plate. *Thin-Walled Struct*. 2021;166:Article 108019.
- [10] Safarpour M, Ebrahimi F, Habibi M, et al. On the nonlinear dynamics of a multi-scale hybrid nanocomposite disk. *Eng Comput*. 2021;37:2369–2388.
- [11] Al-Furjan M, Habibi M, Ghabussi A, et al. Non-polynomial framework for stress and strain response of the FG-GPLRC disk using three-dimensional refined higher-order theory. *Eng Struct*. 2021;228:Article 111496.
- [12] Al-Furjan M, Habibi M, won Jung D, et al. Chaotic responses and nonlinear dynamics of the graphene nanoplatelets reinforced doubly-curved panel. *European J. Mech-A/Solids*. 2021;85:Article 104091.
- [13] Al-Furjan M, Habibi M, Chen G, et al. Chaotic oscillation of a multi-scale hybrid nano-composites reinforced disk under harmonic excitation via GDQM. *Compos Struct*. 2020;252:Article 112737.
- [14] Al-Furjan M, Habibi M, Won Jung D, et al. On the buckling of the polymer-CNT-fiber nanocomposite annular system under thermo-mechanical loads. *Mech Based Des Struct Mach*. 2020;50:1–21.
- [15] Al-Furjan M, Habibi M, Ebrahimi F, et al. A coupled thermomechanics approach for frequency information of electrically composite microshell using heat-transfer continuum problem. *Eur Phys J Plus*. 2020;135:1–45.
- [16] Al-Furjan M, Fereidouni M, Habibi M, et al. Influence of in-plane loading on the vibrations of the fully symmetric mechanical systems via dynamic simulation and generalized differential quadrature framework. *Eng Comput*. 2020;38:1–23.
- [17] Kolekar S, Venkatesh K, Oh J-S, et al. Vibration controllability of sandwich structures with smart materials of electrorheological fluids and magnetorheological materials: a review. *J. Vibrat Eng Techn*. 2019;7:359–377.
- [18] Safa M, Shariati M, Ibrahim Z, et al. Potential of adaptive neuro fuzzy inference system for evaluating the factors affecting steel-concrete composite beam's shear strength. *Steel Compos. Struct*. 2016;21:679–688.
- [19] Shariati A, RamliSulong N, Shariati M. Various types of shear connectors in composite structures: a review. *Int J Phys Sci*. 2012;7:2876–2890.
- [20] Shariati M, Sulong NR, Shariati A, et al. Comparative performance of channel and angle shear connectors in high strength concrete composites: an experimental study. *Constr Build Mater*. 2016;120:382–392.
- [21] Khorramian K, Maleki S, Shariati M, et al. Numerical analysis of tilted angle shear connectors in steel-concrete composite systems. *Steel Compos Struct*. 2017;23:67–85.

- [22] Paknahad M, Shariati M, Sedghi Y, et al. Shear capacity equation for channel shear connectors in steel-concrete composite beams. *Steel Compos Struct.* **2018**;28:483–494.
- [23] Shariati M, Mafipour MS, Mehrabi P, et al. Application of extreme learning machine (ELM) and genetic programming (GP) to design steel-concrete composite floor systems at elevated temperatures. *Steel Compos Struct.* **2019**;33:319–332.
- [24] Halsey TC. Electrorheological fluids. *Science.* **1992**;258:761–766.
- [25] Hao T. Electrorheological fluids. *Adv Mater.* **2001**;13:1847–1857.
- [26] Xu YL, Qu WL, Ko JM. Seismic response control of frame structures using magnetorheological/electrorheological dampers. *Earthq Eng Struct Dyn.* **2000**;29:557–575.
- [27] Wei K, Meng G, Zhou S, et al. Vibration control of variable speed/acceleration rotating beams using smart materials. *J Sound Vib.* **2006**;298:1150–1158.
- [28] Wei K, Bai Q, Meng G, et al. Vibration characteristics of electrorheological elastomer sandwich beams. *Smart Mater Struct.* **2011**;20:Article 055012.
- [29] Vishnu Narayana G, Ganesan N. Critical comparison of viscoelastic damping and electrorheological fluid core damping in composite sandwich skew plates. *Compos Struct.* **2007**;80:221–233.
- [30] Tabassian R, Rezaeepazhand J. Stability of smart sandwich beams with cross-ply faces and electrorheological core subjected to axial loads. *J Reinf Plast Compos.* **2012**;31:55–64.
- [31] Zhao Qianhe, Liu Jin, Yang Haima, et al. Double U-groove temperature and refractive index photonic crystal fiber sensor based on surface plasmon resonance. *Applied Optics.* **2022**;61(24):7225. <http://dx.doi.org/10.1364/AO.462829>.
- [32] Zhao Qianhe, Liu Jin, Yang Haima, et al. High Birefringence D-Shaped Germanium-Doped Photonic Crystal Fiber Sensor. *Micromachines.* **2022**;13(6):826. <http://dx.doi.org/10.3390/mi13060826>.
- [33] Huang Chang-Qin, Jiang Fan, Huang Qiong-Hao, et al. Dual-Graph Attention Convolution Network for 3-D Point Cloud Classification. *IEEE Transactions on Neural Networks and Learning Systems.* **2022**;1–13. <http://dx.doi.org/10.1109/TNNLS.2022.3162301>.
- [34] Gavin HP, Hanson RD, Filisko FE. Electrorheological dampers, part I: analysis and design. *J Appl Mech.* **1996**;63:669–675.
- [35] Yeh J-Y, Chen L-W. Dynamic stability of a sandwich plate with a constraining layer and electrorheological fluid core. *J Sound Vib.* **2005**;285:637–652.
- [36] Gholamzadeh babaki MH, Shakouri M. Free and forced vibration of sandwich plates with electrorheological core and functionally graded face layers. *Mech Based Des Struct Mach.* **2021**;49:689–706.
- [37] Liu Hui, Zhao Yao, Pishbin Mohammad, et al. A comprehensive mathematical simulation of the composite size-dependent rotary 3D microsystem via two-dimensional generalized differential quadrature method. *Engineering with Computers.* **2022**;38(S5):4181–4196. <http://dx.doi.org/10.1007/s00366-021-01419-2>.
- [38] Khaniki HB, Ghayesh MH. A review on the mechanics of carbon nanotube strengthened deformable structures. *Eng Struct.* **2020**;220:Article 110711.
- [39] Gholipour A, Ghayesh MH. Nonlinear coupled mechanics of functionally graded nanobeams. *Int J Eng Sci.* **2020**;150:Article 103221.
- [40] Ghayesh MH. Mechanics of tapered AFG shear-deformable microbeams. *Microsyst Technol.* **2018**;24:1743–1754.
- [41] Rashvand K, Rezazadeh G, Mobki H, et al. On the size-dependent behavior of a capacitive circular micro-plate considering the variable length-scale parameter. *Int J Mech Sci.* **2013**;77:333–342.
- [42] Ghayesh MH. Nonlinear dynamics of multilayered microplates. *J Comput Nonlinear Dyn.* **2018**;13; <https://doi.org/10.1115/1.4037596>.
- [43] Abazid MA. The nonlocal strain gradient theory for hygrothermo-electromagnetic effects on buckling, vibration and wave propagation in piezoelectromagnetic nanoplates. *Int J Appl Mech.* **2019**;11:Article 1950067.
- [44] Ebrahimi F, Barati MR, Dabagh A. A nonlocal strain gradient theory for wave propagation analysis in temperature-dependent inhomogeneous nanoplates. *Int J Eng Sci.* **2016**;107:169–182.
- [45] Karami B, Shahsavari D. Nonlocal strain gradient model for thermal stability of FG nanoplates integrated with piezoelectric layers. *Smart Struct Syst.* **2019**;23:215–225.

- [46] Karami B, Shahsavari D, Janghorban M, et al. On the resonance of functionally graded nanoplates using bi-Helmholtz nonlocal strain gradient theory. *Int J Eng Sci.* **2019**;144:Article 103143.
- [47] Gunasekaran V, Pitchaimani J, Chinnapandi LBM. Analytical investigation on free vibration frequencies of polymer nano composite plate: effect of graphene grading and non-uniform edge loading. *Materials Today Communications.* **2020**;24:Article 100910.
- [48] Lu Siyu, Ban Yuxi, Zhang Xia, et al. Adaptive control of time delay teleoperation system with uncertain dynamics. *Frontiers in Neurorobotics.* **2022**;16:107. <http://dx.doi.org/10.3389/fnbot.2022.928863>.
- [49] Wang Jingwen, Tian Jiawei, Zhang Xia, et al. Control of Time Delay Force Feedback Teleoperation System With Finite Time Convergence. *Frontiers in Neurorobotics.* **2022**;16:107. <http://dx.doi.org/10.3389/fnbot.2022.877069>.
- [50] Ganapathi M, Merzouki T, Polit O. Vibration study of curved nanobeams based on nonlocal higher-order shear deformation theory using finite element approach. *Compos Struct.* **2018**;184:821–838.
- [51] Al-Furjan M, Moghadam SA, Dehini R, et al. Vibration control of a smart shell reinforced by graphene nanoplatelets under external load: semi-numerical and finite element modeling. *Thin-Walled Struct.* **2021**;159:Article 107242.
- [52] Feather WG, Lim H, Knezevic M. A numerical study into element type and mesh resolution for crystal plasticity finite element modeling of explicit grain structures. *Comput Mech.* **2020**;1–23. <https://doi.org/10.1016/j.tws.2020.107242>.
- [53] Wu J, Habibi M. Dynamic simulation of the ultra-fast-rotating sandwich cantilever disk via finite element and semi-numerical methods. *Eng Comput.* **2021**;67.
- [54] Amelirad O, Assempour A. Coupled continuum damage mechanics and crystal plasticity model and its application in damage evolution in polycrystalline aggregates. *Eng Comput.* **2021**;47:1–15.
- [55] Korayem MH, Homayooni A. The size-dependent analysis of multilayer micro-cantilever plate with piezoelectric layer incorporated voltage effect based on a modified couple stress theory. *Eur J Mech A Solids.* **2017**;61:59–72.
- [56] Li C, Han Q, Wang Z, et al. Analysis of wave propagation in functionally graded piezoelectric composite plates reinforced with graphene platelets. *Appl Math Model.* **2020**;81:487–505.
- [57] Shi X, Li J, Habibi M. On the statics and dynamics of an electro-thermo-mechanically porous GPLRC nanoshell conveying fluid flow. *Mech Based Des Struct Mach.* **2020**;81:1–37.
- [58] Xu W, Pan G, Moradi Z, et al. Nonlinear forced vibration analysis of functionally graded non-uniform cylindrical microbeams applying the semi-analytical solution. *Compos Struct.* **2021**;275:Article 114395.
- [59] Ghayesh MH. Nonlinear dynamic response of a simply-supported Kelvin–Voigt viscoelastic beam, additionally supported by a nonlinear spring. *Nonlinear Anal Real World Appl.* **2012**;13:1319–1333.
- [60] Huang Zhiwen, Li Tong, Huang Kexin, et al. Predictions of flow and temperature fields in a T-junction based on dynamic mode decomposition and deep learning. *Energy.* **2022**;261:125228. <http://dx.doi.org/10.1016/j.energy.2022.125228>.
- [61] Ghayesh MH. Nonlinear oscillations of FG cantilevers. *Appl Acoust.* **2019**;145:393–398.
- [62] Reddy J, Wang C, Lee K. Relationships between bending solutions of classical and shear deformation beam theories. *Int J Solids Struct.* **1997**;34:3373–3384.
- [63] Aldraihem OJ, Wetherhold RC, Singh T. Distributed control of laminated beams: Timoshenko theory vs. Euler-Bernoulli theory. *J Intell Mater Syst Struct.* **1997**;8:149–157.
- [64] Timoshenko SP. LXVI. On the correction for shear of the differential equation for transverse vibrations of prismatic bars. *Lond Edinb Dublin Philos Mag J Sci.* **1921**;41:744–746.
- [65] Cowper G. The shear coefficient in Timoshenko's beam theory. 1966.
- [66] Ghayesh MH. Viscoelastic mechanics of Timoshenko functionally graded imperfect microbeams. *Compos Struct.* **2019**;225:Article 110974.
- [67] Li Shuguang, Geng Zhichao. Bicriteria scheduling on an unbounded parallel-batch machine for minimizing makespan and maximum cost. *Information Processing Letters.* **2023**;180:106343. <http://dx.doi.org/10.1016/j.ipl.2022.106343>.

- [68] Khaniki HB, Ghayesh MH, Chin R, et al. Nonlinear continuum mechanics of thick hyperelastic sandwich beams using various shear deformable beam theories. *Continuum Mech Thermodyn*. 2022;34:781–827.
- [69] Moradi H, Atashi P, Amelirad O, et al. Machine learning modeling and DOE-assisted optimization in synthesis of nanosilica particles via Stöber method. *Adv Nano Res*. 2022;12:387–403.
- [70] Guo J, Baharvand A, Tazeddinova D, et al. An intelligent computer method for vibration responses of the spinning multi-layer symmetric nanosystem using multi-physics modeling. *Eng Comput*. 2021. <https://doi.org/10.1080/0305215X.2012.675062>.
- [71] Barretta R, Feo L, Luciano R, et al. Functionally graded Timoshenko nanobeams: a novel nonlocal gradient formulation. *Composites Part B: Engineering*. 2016;100:208–219.
- [72] Liu Hongwei, Shen ShiXin, Oslub Khaled, et al. Amplitude motion and frequency simulation of a composite viscoelastic microsystem within modified couple stress elasticity. *Engineering with Computers*. 2022;38(S5):3977–3991. <http://dx.doi.org/10.1007/s00366-021-01316-8>.
- [73] Kong Fanlei, Dong Fenghui, Duan Maojun, et al. On the vibrations of the Electrorheological sandwich disk with composite face sheets considering pre and post-yield regions. *Thin-Walled Structures*. 2022;179:109631. <http://dx.doi.org/10.1016/j.tws.2022.109631>.
- [74] Safarpour H, Ghanizadeh SA, Habibi M. Wave propagation characteristics of a cylindrical laminated composite nanoshell in thermal environment based on the nonlocal strain gradient theory. *Eur Phys J Plus*. 2018;133:532. <https://doi.org/10.1140/epjp/i2018-12385-2>.
- [75] Shariati A, Habibi M, Tounsi A, et al. Application of exact continuum size-dependent theory for stability and frequency analysis of a curved cantilevered microtubule by considering viscoelastic properties. *Eng Comput*. 2021;37:3629–3648.
- [76] Ebrahimi F, Supeni EEB, Habibi M, et al. Frequency characteristics of a GPL-reinforced composite microdisk coupled with a piezoelectric layer. *Eur Phys J Plus*. 2020;135:1–32.
- [77] Ebrahimi F, Hajilak ZE, Habibi M, et al. Buckling and vibration characteristics of a carbon nanotube-reinforced spinning cantilever cylindrical 3D shell conveying viscous fluid flow and carrying spring-mass systems under various temperature distributions. *Proc Inst Mech Eng Part C J Mech Eng Sci*. 2019;233:4590–4605.
- [78] Oyarhossein MA, Alizadeh Aa, Habibi M, et al. Dynamic response of the nonlocal strain-stress gradient in laminated polymer composites microtubes. *Sci Rep*. 2020;10:1–19.
- [79] Safarpour H, Mohammadi K, Ghadiri M, et al. Effect of porosity on flexural vibration of CNT-reinforced cylindrical shells in thermal environment using GDQM. *Int J Struct Stab Dyn*. 2018;18:Article 1850123.
- [80] Moayedi H, Ebrahimi F, Habibi M, et al. Application of nonlocal strain–stress gradient theory and GDQM for thermo-vibration responses of a laminated composite nanoshell. *Eng Comput*. 2021;37:3359–3374.
- [81] Al-Furjan M, Habibi M, Safarpour H. Vibration control of a smart shell reinforced by graphene nanoplatelets. *Int J Appl Mech*. 2020;12:Article 2050066.
- [82] Lori ES, Ebrahimi F, Supeni EEB, et al. The critical voltage of a GPL-reinforced composite microdisk covered with piezoelectric layer. *Eng Comput*. 2020;12:1–20.
- [83] Huang X, Zhu Y, Vafaei P, et al. An iterative simulation algorithm for large oscillation of the applicable 2D-electrical system on a complex nonlinear substrate. *Eng Comput*. 2021;38:1–13.
- [84] Jiao J, Ghoreishi S-m, Moradi Z, et al. Coupled particle swarm optimization method with genetic algorithm for the static–dynamic performance of the magneto–electro–elastic nanosystem. *Eng Comput*. 2021;38:1–15.
- [85] Ma L, Liu X, Moradi Z. On the chaotic behavior of graphene-reinforced annular systems under harmonic excitation. *Eng Comput*. 2021;38:1–25.
- [86] Liu Y, Wang W, He T, et al. On the modelling of the vibration behaviors via discrete singular convolution method for a high-order sector annular system. *Eng Comput*. 2021;38:1–23.
- [87] Zhao H, Li C, Fu Y, et al. Quasi-static indentation, low-velocity impact, and resonance responses of the laminated double-curved panel considering various boundary conditions. *Thin-Walled Struct*. 2023;183:Article 110360.

- [88] Zheng W, Liu J, Oyarhossein MA, et al. Prediction of nth-order derivatives for vibration responses of a sandwich shell composed of a magnetorheological core and composite face layers. *Eng Anal Boundary Elem.* **2023**;146:170–183.
- [89] Zhang W, Liu Z, Liang Z, et al. A comprehensive computer simulation of the size-dependent sector or complete microsystem via two-dimensional generalized differential quadrature method. *Eng Comput.* **2021**;38:1–17.
- [90] Zhu Lei, Ren Hao, Habibi Mostafa, et al. Predicting the environmental economic dispatch problem for reducing waste nonrenewable materials via an innovative constraint multi-objective Chimp Optimization Algorithm. *Journal of Cleaner Production.* **2022**;365:132697. <http://dx.doi.org/10.1016/j.jclepro.2022.132697>.
- [91] Wang Zhiyong, Yu Shuiqin, Xiao Zhixiong, et al. Frequency and buckling responses of a high-speed rotating fiber metal laminated cantilevered microdisk. *Mechanics of Advanced Materials and Structures.* **2022**;29(10):1475–1488. <http://dx.doi.org/10.1080/15376494.2020.1824284>.
- [92] Li S, Geng Z. Bicriteria scheduling on an unbounded parallel-batch machine for minimizing makespan and maximum cost. *Inf Process Lett.* **2023**;180:Article 106343.
- [93] Chen Fujiang, Chen Junying, Duan Rongqian, et al. Investigation on dynamic stability and aeroelastic characteristics of composite curved pipes with any yawed angle. *Composite Structures.* **2022**;284:115195. <http://dx.doi.org/10.1016/j.compstruct.2022.115195>.
- [94] Shao Yunhong, Zhao Yang, Gao Jun, et al. Energy absorption of the strengthened viscoelastic multi-curved composite panel under friction force. *Archives of Civil and Mechanical Engineering.* **2021**;21(4)<http://dx.doi.org/10.1007/s43452-021-00279-3>.
- [95] Yeh J-Y, Chen L-W, Wang C-C. Dynamic stability of a sandwich beam with a constrained layer and electrorheological fluid core. *Compos Struct.* **2004**;64:47–54.
- [96] Allahverdizadeh A, Mahjoob M, Maleki M, et al. Structural modeling, vibration analysis and optimal viscoelastic layer characterization of adaptive sandwich beams with electrorheological fluid core. *Mech Res Commun.* **2013**;51:15–22.
- [97] Arikoglu A, Ozkol I. Vibration analysis of composite sandwich beams with viscoelastic core by using differential transform method. *Compos Struct.* **2010**;92:3031–3039.
- [98] Tang S-J, Lumsdaine A. Analysis of constrained damping layers, including normal-strain effects. *AIAA J.* **2008**;46:2998–3011.